Geology and tectono-metamorphic evolution of the Himalayan metamorphic core: Insights from the Mugu Karnali transect, Western Nepal (Central Himalaya)

Journal of METAMORPHIC GEOLOGY

Geology and tectono-metamorphic evolution of the Himalayan Metamorphic Core: insights from the Mugu Karnali transect, Western Nepal (Central Himalaya)

Journal:	*Journal of Metamorphic Geology*
Manuscript ID	JMG-16-0042.R1
Manuscript Type:	Original Article
Date Submitted by the Author:	04-Oct-2016
Complete List of Authors:	Iaccarino, Salvatore; Universita degli Studi di Pisa, Scienze della Terra Montomoli, Chiara; Università di Pisa, Dipartimento di Scienze della Terra Carosi, Rodolfo; Università di Torino, Scienze della Terra Massonne, Hans-Joachim; Universität Stuttgart, Institut für Mineralogie und Kristallchemie Visonà, Dario; Universita degli Studi di Padova, Dipartimento di Geoscienze
Keywords:	Greater Himalayan Sequence; Himalayan metamorphic core; pseudosection; Himalayan tectonics; Western Nepal geology

Geology and tectono-metamorphic evolution of the Himalayan Metamorphic Core: insights from the Mugu Karnali transect, Western Nepal (Central Himalaya)

Iaccarino S.[1], Montomoli C.[1], Carosi R.[2], Massonne H.–J.[3] and Visonà D.[4]

Affiliations:

[1]*Dipartimento di Scienze della Terra, Università di Pisa, via S. Maria, 53, 56126 Pisa, Italy, salvatore.iaccarino@dst.unipi.it*

[2]*Dipartimento di Scienze della Terra, Università di Torino, via Valperga Caluso, 35, 10125 Torino, Italy*

[3]*Institut für Mineralogie und Kristallchemie, Universität Stuttgart, Azenbergstrasse 18, 70174, Stuttgart, Germany.*

[4]*Dipartimento di Geoscienze, Università di Padova, via Gradenigo, 6, 35131, Padova, Italy*

ABSTRACT

We present new structural and tectono-metamorphic data from a geological transect along the Mugu Karnali valley, in Western Nepal (Central Himalaya), where an almost continuous cross section from the Lesser Himalaya Sequence to the Everest Series through the medium-high-grade Greater Himalayan Sequence (GHS) is exposed. Detailed meso- and micro-structural analyses were carried out along the transect. Pressure (P) -temperature (T) conditions and *P-T*-deformation paths for samples from different structural units were derived by calculating pseudosections in the MnNKCFMASHT system. Systematic increase of *P-T* conditions, from ~ 0.75 GPa–560 °C up to ≥1.0 GPa–750°C have been detected starting from the garnet zone up to the K-feldspar + aluminosilicate zone. Our investigation reveals how these units are characterized by different evolutions and well-developed tectonic boundaries. Integrating our meso- and micro-structural data with those of metamorphism and geochronology, a diachronism in deformation and metamorphism

can be highlighted along the transect, where different crustal slices were underthrust, metamorphosed and exhumed at different times.

The GHS is not a single tectonic unit, but it is composed of (at least) three different crustal slices, in agreement with a model of in-sequence shearing by accretion of material from the Indian plate, where coeval activity of basal thrusting at the bottom with normal shearing at the top of the GHS is not strictly required for its exhumation.

Key words: Greater Himalayan Sequence; Himalayan metamorphic core; pseudosection; Himalayan tectonics; Western Nepal geology

INTRODUCTION

The Himalayan range, extending for over 2400 km (Fig. 1), played a central role in shaping ~~our~~ understanding on the formation of mountains belt due to the collision of continental plates (Kohn, 2014 and references therein). In spite of its apparent structural simplicity several geodynamic processes, which are currently among the major topics in geosciences, have been developed ~~looking to~~ the Himalayas, such as: *(i)* syn-convergence extension along crustal scale detachment coeval with basal thrusting at the South Tibetan Detachment System (STDS) and Main Central Thrust (MCT) and its implications on the exhumation of deep-seated crustal rocks *i.e.* the Greater Himalayan Sequence (GHS, *e.g.* Teyssier, 2011); *(ii)* feedback relations between climate, crustal melting and tectonics (*e.g.* Jamieson & Beaumont, 2013).

Notwithstanding this progress, there are several Himalayan areas where the present geological knowledge is still very poor. Western Nepal, in the Central Himalaya, is among these areas, even if several important contributions are published (*e.g.* Hagen, 1969; Fuchs, 1974, 1977; Arita *et al.,* 1984; Robinson *et al.,* , Carosi *et al.,* , 2007, 2010; Yakymchuk & Godin, 2012; Montomoli *et al.,* 2013).

In Western Nepal two recent findings newly opened the discussion on exhumation mechanisms of crystalline rocks in the Himalayas: *(i)* Bertoldi *et al.* (2011) and Carosi *et al.* (2013) described a large (~110 km^2) Higher Himalayan leucogranite (HHL), named Bura Buri granite, which intruded the upper part of the GHS up to the low grade Tethyan Sedimentary Sequence (TSS) at *c.* 24-23 Ma (zircon and monazite, U-Pb ages). These data constrain that the STDS age is older than *c.* 24 Ma in this transect. *(ii)* Montomoli *et al.* (2013, 2015) described the kinematics, timing and metamorphic consequences of a high temperature (HT) shear zone occurring within the core of the GHS, called Mangri Shear Zone (MSZ). These findings, in conjunction with others (*e.g.* Carosi *et al.,* 2010; Larson *et al.,* 2013; [illegible]ang *et al.,* 20[illegible], [illegible]accarino *et al.,* 20[illegible]), reveal the structural complexity of the GHS (*e.g.* [illegible]ntomoli *et al.,* 2015; [illegible]ottle *et al.,* 2015).

In this contribution, we describe the main geological features along a structural transect in the Mugu Karnali Valley (Western Nepal, Fig. 1) presenting new structural and metamorphic data of this poorly investigated area (Fig. 1c) where, despite the previous contributions (Bertoldi *et al.* 2011; Carosi et al., 2013; Montomoli et al., 2013), a complete structural and [illegible]profile is still lacking. Moreover, combining [illegible]lata with available geochronological data for this transect and nearby areas, we constrain the tectono-metamorphic evolution of the Himalayan metamorphic core (HMC) in this area. We also discuss the tectonic and geodynamic implications of these findings in the light of the results by Carosi *et al.* (2013, 2016) and Montomoli *et al.,* (2013, 2015).

GEOLOGICAL BACKGROUND

The Himalayan belt (Fig. 1a) is mainly composed of continuous packages of imbricated litho-tectonic units (Le Fort, 1975; Hodges, 2000). Among these units, the GHS (Fig. 1), made of medium- to high-grade metamorphic rocks and Cenozoic leucogranites (HHL, Visonà *et al.,* 2012), represents the exhumed mid-crustal core of the Himalaya (Hodges, 2000; Cottle *et al.,* 2015). Classically, GHS rocks have been subdivided in three main "formations" (Le Fort, 1975), now referred as units (*e.g.* Searle & Godin, 2003). The structurally lower one, Unit 1, consists of garnet-

and kyanite-bearing metapelite, subordinate quartzite, calcsilicate, migmatite and marble. The structurally intermediate Unit 2 is composed of medium to high-grade calcsilicate, minor marble and metapelite. The structurally highest Unit 3 consists of orthogneiss and kyanite/sillimanite-bearing migmatite, with minor calcsilicate gneiss.

Two main peculiarities in the GHS have been described (Hodges 2000 and references therein): *(i)* the recognition of an inverse metamorphic field gradient with high-grade "Barrovian" minerals appearing structurally upward (Le Fort, 1975). *(ii)* the fact that the GHS is tectonically bounded by two crustal scale shear zones with opposite sense of shear: a basal ductile to brittle reverse shear zone, the MCT (*e.g.* Heim & Gansser 1939), thrusting the GHS above the Lesser Himalaya Sequence (LHS) made of medium- to low-grade metamorphic rocks (Hodges, 2000) of Palaeoproterozoic-Mesoproterozoic age (Upreti, 1999); and an upper, ductile to brittle detachment system of normal faults, the STDS (Burg *et al.,* 1984; Carosi *et al.,* 1998), through which Cambrian (?) to Eocene (*e.g.* Garzanti, 1999 and reference therein) sedimentary rocks of the Tethyan Sedimentary Sequence (TSS) are tectonically juxtaposed above the GHS.

Metamorphism in the GHS has been classically subdivided in two main stages (*e.g.* Vannay & Hodges, 1996; Hodges, 2000). The older one is the Eocene-Oligocene Eohimalayan stage, where high-pressure (kyanite-bearing) assemblages developed (Vannay & Hodges, 1996; Iaccarino *et al.,* 2015). It was followed by the Neohimalayan stage starting in the Early Miocene. Medium- to low-pressure (sillimanite to cordierite) bearing assemblages, extensive melting (HHL production), and coeval slip along the STDS and MCT (*e.g.* Godin *et al.,* 2006 and references therein) characterize this stage. Some authors (e.g. Cottle et al., 2015) refer collectively to the pervasively deformed and metamorphosed rocks during the India-Asia continental collision as the Himalayan Metamorphic Core (HMC).

MUGU KARNALI: A GEOLOGICAL TRANSECT

The Mugu Karnali valley (Figs 1b,c) trends nearly E-W and provides about 30-40 km of nearly continuous outcrops along the main tectono-metamorphic units (Montomoli *et al.,* 2013). The area was partly mapped in the 1970's by Fuchs and co-workers (e.g. Fuchs, 1974, 1977 and references therein).

In this contribution a detailed structural and metamorphic map is presented (Figs 1c & 2). The distribution of isograd-minerals is based on the "first Barrovian mineral appearance/disappearance" integrating field observations with optical/scanning-electron microscope data from over 200 thin sections. The general architecture is represented by a NE-E dipping homoclinal slab (Fig. 2). The lower tectonic unit, the LHS, is composed of quartzite with preserved primary structures, marble, dolomitic marble, graphitic schist and minor metabasite. The LHS main foliation ($S_{P(LHS)}$), parallel to the axial plane of tight to isoclinal folds, strikes NW-SE and dips to NE (Fig. 1c). Meso- and micro-structural analyses reveal that the $S_{P(LHS)}$ is a second phase foliation since relicts of an older continuous to spaced foliation ($S_{P-1(LHS)}$) are recognizable both at the meso- and at the microscale. The mineral and aggregate lineation ($L_{P(LHS)}$) generally trends NE-SW and moderately plunges to the NE (Fig. 1c). Deformation and metamorphism increase structurally upward, with the development of L-tectonite, defined by the alignment of chlorite within LHS quartzite (Fig. 2a) and the development of garnet-chlorite-biotite bearing phyllite (Grt I zone) just below the tectonic contact between the LHS and the GHS ( ). This contact, in the studied area, is neither a sharp fault nor a protolith boundary (see also Carosi *et al.,* 2007; Searle *et al.,* 2008), but it is a large (several km thick) ductile shear zone affecting both quartzite and garnet-biotite bearing phyllites (Grt II zone) and higher grade metamorphic rocks of the GHS. For this reason, we refer to this high strain zone as Main Central Thrust Zone (MCTZ in , Carosi *et al.,* 2007). Within the MCTZ a NW-SE striking mylonitic foliation is developed and kinematic indicators such as S-C-C' fabric, asymmetric porphyroclasts and quartz sigmoids point to a top-to-the W-SW sense of shear (Fig. 1c) occur. The main GHS foliation ($S_{P(GHS)}$), dipping mainly toward E (Fig. 1c) strikes NW-SE and NNE-SSW when moving upward in the section. An older foliation ($S_{P-1(GHS)}$) is sporadically

observed both at the meso- and microscale. The mineral lineation ($L_{P(GHS)}$) trends mainly NE-SW and plunges moderately to the E-NE (Fig. 2c). An inverse metamorphic gradient is observed in the field within the GHS (Figs 1c & 2) and confirmed by the study of thin-sections starting from garnet-biotite-bearing rocks up to garnet-kyanite-biotite paragneiss and sillimanite-bearing gneiss, moving structurally upward.

Following Larson *et al.* (2010) the GHS in the study area has been subdivided (Figs 1c & 2) into the lower GHS (GHS_L) and the upper GHS (GHS_U). These subunits are separated by a tectono-metamorphic discontinuity (MSZ) described in detail by Montomoli *et al.* (2013). It is worthy of note that this subdivision is different from the one proposed by Fuchs (1977) who mapped two main crystalline nappes, a Lower Crystalline Nappe, roughly between Gamgadhi and Kumpha villages (included now mainly in the MCTZ, Fig. 1c), and an Upper Crystalline Nappe (from Kumpha up to the E) only partially mapped by the former author (now a part of the GHS).

The GHS_L consists mainly of quartzite, metapelite and orthogneiss, with minor calcsilicate and amphibolite (Fig. 2b,c). The first appearance of sillimanite, as rare fibrolite, has been recognized within orthogneiss SW of the village of Mangri (Fig. 1c). Here, cuspate-lobate structures between competent orthogneiss and less competent metapelite and tourmaline-bearing leucocratic magmatic pods and minor anatectites occur. Structurally upward, mylonitic gneiss and micaschist of the MSZ mark the bottom of the GHS_U (Figs 2d,e) which contains sillimanite + white mica-bearing paragneiss and micaschist, K-feldspar + aluminosilicate-bearing migmatite, HHL and minor clinopyroxene-bearing calcsilicate. Relicts of kyanite, partially replaced by sillimanite have been detected.

A newly identified, HT contractional shear zone, named Tiyar Shear Zone (TSZ) (Figs 1c & 2), marks the base of the migmatitic complex. The appearance of the TSZ coincides with the disappearance of white mica (aluminosilicate + K-feldspar isograd). The main mylonitic foliation, reworking the migmatitic fabric (Fig. 2d), is concordant with that one of the host gneisses. The stretching lineation, marked by sillimanite and quartzo-feldspathic grains, dips to the E-NE (Fig.

153 1c). Top-to-the W-SW kinematic indicators such as quartzo-feldspathic sigmoidal pods (Fig. 2d), S-
154 C fabric, garnet and K-feldspar porphyroclasts occur in the TSZ.
155 The migmatitic complex is made of stromatic metatexite (with minor diatexite) with alternations of
156 leucosome and melanosome, both containing garnet and aluminosilicate (Figs 2e & 3a,b).
157 Leucocratic veinlets discordant to the main foliation are also observed (Fig. 3b). The truly anatectic
158 nature of these rocks, besides field observations, is supported by observations on thin sections.
159 Typical (*e.g.* Vernon, 2011) microstructures of melt-bearing rocks are observed (Figs 3c-f), such as:
160 (i) euhedral crystals (*e.g.* feldspar) interpreted as precipitated from a melt (Figs 3a,c); (ii) corroded
161 quartz grains rimmed by feldspar forming tiny films with low dihedral angles, interpreted as melt
162 pseudomorphs (Fig. 3d); (iii) clusters of tiny poly-mineralic, K-feldspar-bearing inclusions, that are
163 likely nanogranitoids (Cesare B., personal communication, 2014; *e.g.* Bartoli et al., 2016) within
164 peritectic garnet (Fig. 3f). The migmatitic complex is intruded on the northern side of the mapped
165 area by a pluri-kilometric leucogranite, the Mugu granite (Figs 1c & 2), which is often referred in
166 the geological literature as Mugu-Dolpo-Mustang granite (*e.g.* Le Fort & France-Lanord, 1995),
167 although its continuity from the Dolpo-Mustang region to the Mugu area has not been demonstrated
168 yet. The Mugu leucogranite contains K-feldspar-plagioclase-quartz-white mica-biotite ± tourmaline
169 ± garnet typical for peraluminous granites. Few geochronological data are available for the Mugu-
170 Dolpo-Mustang granite: Harrison *et al.* (1999) reported an age of 17.6 ± 0.3 Ma (Th-Pb on
171 monazite); Guillot *et al.* (1999) published white mica and biotite Ar-Ar ages of *c.* 17-15 Ma. These
172 geochronological results refer to sample locations, which are more than 100 km away from the
173 Mugu *sensu stricto* granite.
174 South of the Mugu granite (Fig. 1c), structurally above the migmatitic complex, leucogranitic dyke
175 swarms intrude intercalations of calcsilicate and low-grade biotite-bearing metapsammopelite. The
176 main foliation strikes ENE-WSW dipping towards S-SE (Fig. 1c). Mineral lineations defined by
177 biotite are present with an ENE-WSW trend plunging to the SW. The base of these rocks is strongly
178 deformed with zoned calcsilicates showing symmetric and asymmetric boudins. Observations on

two orthogonal outcrop surfaces suggest a strain pattern typical of field I of Ramsay & Huber (1983). Rare kinematic indicators such as flanking folds (Fig. 2f), point to a top to the S/SE sense of shear. This situation is comparable with the one on the southern side (Fig. 1c) of the studied area, where the Bura Buri granite (Bertoldi *et al.,* 2011; Carosi *et al.,* 2013) intrudes garnet-cordierite (after staurolite)-two mica-bearing gneiss, which can be correlated with the Everest Series (ES) of Jessup *et al.*, (2008), low-grade marble and "lumachelle" limestone of the TSS. Due to the closeness to the Tibetan border, it has not been possible to fully map the Mugu granite and to constrain its relationships with the STDS and TSS, as it was done for the Bura Buri granite (Bertoldi *et al.,* 2011; Carosi *et al.,* 2013).

A late ductile deformation event, affecting heterogeneously the whole GHS-LHS, re-folds the main foliation to upright folds often with kink-like geometry. However, a clear syn-kinematic mineral recrystallization on the axial plane-related foliation (S_{p+1}) was not developed.

In order to constrain the pressure (P) - temperature (T) - deformation (d) evolution of the HMC along the Mugu Karnali transect, five representative samples, with clear mineral growth-deformation relationships, from the different structural units (Figs 1c & 2) have been selected for a detailed study.

SELECTED SAMPLES: MICROSTRUCTURES AND MINERAL CHEMISTRY

Methods

Thin sections of selected samples, according to their structural position (D13-series as well as D09-10 and D09-52 described by Montomoli *et al.,* 2013), were prepared parallel to the XZ plane of the corresponding finite strain ellipsoid. We used these sections for analyses of minerals with a CAMECA SX100 electron microprobe (EMP) equipped with five wavelength dispersive spectrometers (WDS) at Universität Stuttgart. The EMP energy dispersive system (EDS) was used for qualitative identification of minerals. Chemical compositional maps (X-ray maps) were acquired on at least two selected areas for mica and garnet per specimen applying a stepwise movement (100

ms per step), a beam current of 60 nA for garnet and 30 nA for micas, and a subsequent computer-aided evaluation. Yttrium, Ca, Mn, Fe, Mg were chosen for garnet, whereas Ba, Na, Mg, Fe, Ti were selected for micas. The applied acceleration voltage and beam current for spot analysis were 15 kV and 30 nA for garnet, and 15 kV and 10 nA for the other minerals. This type of analysis lasted ~ 2 minutes. For analyzing Zr in rutile and Y in garnet a beam current of 100 nA and an acceleration voltage of 15 kV were selected. Synthetic and natural standards were used for the calibration of the EMP (see also Massonne, 2012, for the analytical errors). Mineral structural formulae were calculated with the software CALCMIN (Brandelik, 2009). Representative garnet compositional maps are given in Fig. 4; compositional variations of the main silicates are summarized in Fig. 5 and discussed below. Selected analyses are reported in Tables 1-4. Mineral abbreviations used in the text and figures are as follow: And = andalusite, Bt = biotite, Chl = chlorite, Crd = cordierite, Cpx = clinopyroxene, Grt = garnet, Ilm = ilmenite, Kfs = K-feldspar, Ky = kyanite, L = melt, Lws = lawsonite, Opx = orthopyroxene, Pl = plagioclase, Pg = Na-Ca white mica, Qz = quartz, Rt = rutile, Sil = sillimanite, St = staurolite, Ttn = titanite, V = H_2O fluid, Wm = K-white mica, Zo = zoisite.

.

Sample D13-75 (LHS: Grt I zone)

Sample D13-75 is a phyllite from the top of the LHS (Figs 1c & 2) with the assemblage chlorite-white mica-quartz-garnet-plagioclase-biotite-ilmenite (± tourmaline, apatite, zircon). This rock is characterized by alternations of granoblastic and lepidoblastic layers (Figs 6a,b). The main foliation, $S_{P(LHS)}$ (Fig 6a,c) defined by micas and quartz grain shape preferred orientation (GSPO), could be classified as crenulation cleavage (Passchier & Trouw, 2005). An earlier continuous to spaced cleavage, $S_{P-1(LHS)}$ defined by micas, is preserved within the microlithons (Fig 6a,b). Large porphyroblasts of garnet (Fig. 6a), plagioclase and minor biotite occur (Fig. 6b), often with an internal foliation (S_i) defined mainly by ilmenite, quartz, plagioclase and micas. Relationships between S_i and $S_{P(LHS)}$, suggest that garnet, plagioclase and biotite could be interpreted as early-syn-

to syn-tectonic porphyroblasts with respect to the deformational event related to $S_{P(LHS)}$. Texturally late, retrograde chlorite filled garnet fractures or partially replaced biotite. Quartz in the sample shows evidence of grain boundary migration (GBM) recrystallization (Law, 2014 and references therein) such as lobate grain boundaries and pinning of micas. Moreover, deformation lamellae heterogeneously occur testifying that deformation continued after temperature peak (Passchier & Trouw, 2005). Post-kinematic white mica and biotite sporadically overgrew the main foliation.

Mineral chemistry and garnet zoning

Garnet shows a gradual decrease of Mn, balanced by an increase of Mg, from core (center: XMn = Mn/(Mn+Mg+Ca+Fe)=0.17-0. 16, XCa=0.19-0.18, XMg=0.03-0.04, and XFe = 0.62) to the rim (XMn = 0.02, XCa= 0.18, XMg= 0.08-0.07, XFe=0.72; Figs 4 & 5a; Table 1) typical for a prograde growth zoning (*e.g.* Tracy *et al.,* 1979; Spear, 1993). The Fe/(Fe+Mg) ratio (hereafter Fe#) varies from 0.95 in the core to 0.91 for the rim.

Plagioclase (Fig. 5b; Table 2) is mainly oligoclase with XAb (= Na/(Na+Ca+K)) between 0.69 and 0.81. Nearly pure albite (XAb=0.99) has been found in some sporadic inclusions within garnet.

Biotite is quite homogeneous in composition with XMg (=Mg/(Mg+Fe))=0.46-0.48 and Ti a.p.f.u. (= atoms per formula unit, on 11 O basis) between 0.08-0.11 (Fig. 5c; Table 3). White mica is compositionally variable with Si a.p.f.u. between 3.06 and 3.16, with the highest values obtained for grains aligned along the main foliation (Fig. 5d; Table 4). Chlorite has XMg between 0.43 and 0.48 with the lowest values observed in garnet inclusions.

Sample D13-06 (GHS_L: Grt II zone)

Sample D13-06 is a metapsammite from the medium-upper part of the MCTZ (Grt II zone; Figs 1c & 2) with the assemblage white mica-biotite-garnet-quartz-plagioclase-ilmenite (± tourmaline, apatite, zircon, monazite and xenotime). The rock shows an anastomosing disjunctive mylonitic

256 foliation (Passchier & Trouw, 2005) defined by white mica, biotite and ilmenite and by
257 quartz/feldspar GSPO (Fig. 6c).
258 Garnet is present as a skeletal porphyroblast, embayed in a quartz matrix (Fig. 6c), and it is
259 wrapped by the mylonitic foliation. Sporadic S_i, defined by quartz iso-orientation, is discordant to
260 concordant with the external one, suggesting that garnet could be an intertectonic to early-
261 syntectonic porphyroblast (Passchier & Trouw, 2005). Late chlorite is present (in low modal
262 amount) partially replacing biotite or garnet edges (Fig. 6c). Well-developed kinematic indicators
263 such as S-C fabric and asymmetric strain shadows (Fig. 6c) point to a general top-to-the SW sense
264 of shear (Fig. 6a), in agreement with field observations. Quartz shows evidences of GBM dynamic
265 recrystallization.
266
267 *Mineral chemistry and garnet zoning*
268 Garnet X-ray maps show evidence for diffusionally modified growth domains (Fig. 4) with hardly
269 discernable zoning and a discontinuous enrichment of Mn towards the outermost rims (XMn=0.07-
270 0.06; XCa=0.13-0.12; XMg=0.64; Fe#=0.93). This feature points to late resorption of garnet (Kohn
271 & Spear, , Spear,). XAb in plagioclase ranges between 0.77 and 0.90 with the lowest
272 values in inclusions in garnet (Fig. 5b; Table 2). Biotite shows XMg between 0.35 and 0.39 and Ti
273 a.p.f.u. between 0.05 and 0.17, with the lowest values obtained from biotite inclusions in garnet
274 (Fig. 5c; Table 3). The contents of Si a.p.f.u. in white mica vary between 3.09 and 3.25 (Fig. 5d;
275 Table 4). The late chlorite has XMg between 0.39 and 0.41.
276
277 **Sample D09-10 (GHS_L: St + Bt ± Ky zone)**
278 Sample D09-10 is a paragneiss from the GHS_L (see also Montomoli *et al.*, 2013), where staurolite
279 coexists with biotite (± kyanite) (Figs 1c & 2). The assemblage (Fig. 6d) is characterized by white
280 mica-biotite-garnet-staurolite-kyanite-plagioclase-quartz (± tourmaline, Ti-oxides, graphite, apatite,
281 zircon, monazite and xenotime), where the micas define the main foliation, $S_{P(GHS)}$, classified as an

anastomosing disjunctive schistosity (Passchier & Trouw, 2005). Moreover, relicts of an older continuous to spaced schistosity, $S_{P\text{-}1(GHS)}$, defined by oriented white mica and biotite, were sporadically detected.

Garnet porphyroblasts (Fig. 6d) show an inner/intermediate domain, where inclusions (often classified as growth inclusions *sensu* Passchier & Trouw, 2005) of ilmenite, quartz, chlorite, white mica, biotite, graphite, ± Na-Ca white mica, ± rutile, ± xenotime, ± monazite are abundant, and an inclusion-poor rim. Occasionally, S_i in garnet (Fig. 6d) is discordant to the external foliation. Staurolite contains inclusions of quartz, white mica, biotite, plagioclase, ilmenite/rutile, graphite, garnet (Fig. 6f), ± tourmaline, defining an S_i, that is quite often curved and in continuity (Fig. 6e) with the external main foliation ($S_{P(GHS)}$). Kyanite is aligned along the main foliation $S_{P(GHS)}$, sometimes kinked, and partially replaced by white mica (Fig. 6d). Interestingly, rutile surrounded by ilmenite was found in the matrix and enclosed in staurolite. Following the aforementioned textures, garnet is interpreted as inter- to early- syn-tectonic, kyanite as early-syn-tectonic, and staurolite as early-syn- to syn-tectonic porphyroblasts (Passchier & Trouw, 2005). Late retrograde chlorite partially replaced garnet and biotite. Quartz shows evidence of the GBM dynamic recrystallization regime. Annealed grains with straight triple points are also sometimes present. Feldspar shows evidences of ductile deformation by undulose extinction and deformation twins.

Mineral chemistry and garnet zoning

Garnet presents clear evidence of prograde growth zoning (Figs 4 & 5a; Table 1) by the systematic decrease of Mn and Ca, balanced by increase of Mg and Fe from core (XMn=0.[redacted]1, XCa=[redacted], XMg=0.35–0.32, XFe=0.68–0.65, Fe#=0.95-0.94) to the inner rim (XMn=0.008–0.004, XCa=0.71–0.04, XMg=0.12–0.11, XFe=0.84–0.81, Fe#=0.85–0.84). A thin outermost rim (Fig. 4) with Mn (XMn up to 0.014) and Fe# (=0.86–0.88) enrichment suggests minor garnet resorption and re-equilibration. Plagioclase (Table 2) shows generally higher XAb when included in garnet (XAb=0.60-0.90, Fig. 5b) compared to matrix grains (XAb=0.87-0.91). Biotite inclusions in

garnet (Table 3) show lower Ti a.p.f.u. (0.05-0.08) and XMg (0.39-0.50) with respect to biotite defining the main foliation (Ti a.p.f.u.=0.08-0.10, XMg=0.45-0.59). White mica is characterized by Si a.p.f.u. between 3.21 and 3.08, with the lowest values analyzed in mica enclosed in garnet (Table 4). Na-Ca white mica, observed only in garnet, is margarite-rich with Na/(Na+Ca) of 0.20. XMg of staurolite is between 0.18 and 0.16, with the lowest values obtained from the rims.

Sample D09-52 (GHS_U: Als + Wm zone)

Sample D09-52 is a mylonitic paragneiss from the Mangri Shear Zone (see also Montomoli *et al.*, 2013), defining the base of the GHS_U (Figs 1c & 2). The observed assemblage (Fig. 7a) is biotite-garnet-white mica-sillimanite-quartz-plagioclase (± tourmaline, Ti-oxides, apatite, monazite, zircon and xenotime). The main foliation, $S_{P(GHS)}$, is an anastomosing disjunctive mylonitic schistosity (Passchier & Trouw, 2005) defined by biotite, sillimanite, white mica and ilmenite (Fig. 7a). This sillimanite-bearing mylonitic foliation (Fig. 7a) wraps around garnet porphyroclasts (Fig. 7a), which sometimes show an S_i, traced by quartz, plagioclase, mica and rutile, being discordant to the external one (*i.e.* intertectonic garnet). In addition, this foliation envelops large kinked white mica porphyroclasts (Fig. 7b), which can also display an S_i traced by quartz, biotite and rutile. Late chlorite partially replaces garnet edges and biotite. Quartz shows evidence of a dynamic recrystallization regime (Montomoli *et al.,* 2013), such as chessboard extinction and lobate grain boundaries (GBM_{II}, Law, 2014). Kinematic indicators, such as S-C fabric and mica fishes, point to a top-to-the W-SW sense of shear (Fig. 7a,b).

Mineral chemistry and garnet zoning

Garnet X-ray maps show a zoning with a strong decrease of Ca, coupled with a slight decrease of Mn and a slight increase of Mg from core (XMn=0.07–0.05, XCa=0.10–0.07, XMg=0.12-0.10, XFe=, Fe#=0.88–0.87) to inner rim (XMn=0.03–0.02, XCa=0.05–0.03, XMg=0.15–0.09, Fe#=0.85–0.84). A clear discernable outermost rim (Fig. 4; Table 1) with high Mn (XMn up to

334 0.11) and Fe# (=0.91) suggests garnet resorption via retrograde net-transfer reactions (Kohn &
335 Spear, 2000). Plagioclase is characterized by XAb of 0.71-0.85 (Table 2), with the lowest values
336 found in plagioclase within garnet inclusions (Fig. 5b). Matrix biotite shows XMg of 0.34-0.38 and
337 Ti a.p.f.u. between 0.15 and 0.18. Biotite enclosed in garnet is characterized by XMg of 0.52-0.45
338 and Ti a.p.f.u. between 0.09 and 0.15 (Fig. 5c; Table 3). White mica (Fig. 5d) shows Si a.p.f.u. in
339 the range of 3.25-3.10, with the highest values analyzed in large mica fish (Table 4; see also
340 Montomoli *et al.*, 2013).
341
342 **Sample D13-28 (GHS_U: Als + Kfs zone)**
343 Sample D13-28 is from the mesosome of sheared migmatites forming the Tiyar Shear Zone (Figs 1c
344 & 2d). This sample contains K-feldspar-garnet-aluminosilicate-plagioclase-quartz-biotite-
345 rutile/ilmenite ±white mica (+melt) with apatite, monazite and zircon as accessories. A spaced
346 anastomosing mylonitic schistosity, defined by biotite and sillimanite (Fig. 7c-f), wraps around
347 garnet and K-feldspar porphyroclasts (Fig. 7c-f). Garnet contains K-feldspar inclusions in the
348 outermost domain, testifying that at least a part of the garnet is peritectic in origin, since both
349 phases coexist as products of mica-consuming melt-forming reactions (*e.g.* Groppo *et al.*, 2012 and
350 references therein). The margin of garnet is replaced by sillimanite+biotite (Fig. 7f). Kyanite is
351 deformed (Figs 7d,e), sometimes boudinaged with sillimanite filling the necking. Rutile occurs
352 enclosed in garnet and K-feldspar and in the matrix, where it is often partially replaced by ilmenite.
353 These microstructural observations (Figs 7c-f) suggest that the "peak" pre-mylonitic assemblage
354 (hereafter M1) was K-feldspar-garnet-kyanite-plagioclase-quartz-biotite-rutile (+melt), whereas the
355 "post peak", syn-mylonitic assemblage (hereafter M2) is K-feldspar-garnet-sillimanite-plagioclase-
356 quartz-biotite-ilmenite ±white mica/melt.
357 Microstructures suggest a HT deformation regime supported by quartz, forming strain-free ribbons
358 (Figs 7c,d), and a uniform feldspar-quartz recrystallized matrix with interlobate grain-boundaries
359 (Figs 7c,d). K-feldspar (Fig. 7c) shows evidences of ductile dynamic recrystallization such as a core

and mantle structure, myrmekite and perthitic exsolution. Garnet ellipsoid shape (Fig. 7f), suggesting its possible ductile behavior, is also compatible with the invoked HT deformation regime (Passchier & Trouw, 2005). Late white mica forms large flakes (Fig. 7c), crosscutting the mylonitic foliation, or tiny grains oriented along this foliation.

Kinematic indicators such as asymmetric porphyroclasts (Fig. 7c), asymmetric myrmekite (Fig. 7c), and kyanite fishes (Fig. 7d) point to a top-to-the W-SW sense of shear.

Mineral chemistry and garnet zoning

Garnet shows a zoning especially in Ca (Figs 4 & 5a; Table 1). The core is richer in Ca and poorer in Mg (XCa=0.19–0.12; XFe=0.71–0.67; XMn=0.06–0.04; Fe#=0.87–0.86) compared to the inner rim (XCa=0.11–0.05; XFe=0.77–0.74; XMn=0.06–0.04; Fe#=0.91–0.87). An increase of XMn (=0.08–0.11), as well as of Fe# (=0.93–0.91), at the outermost rim domain points to garnet resorption (Kohn & Spear, 2000). However, as described above, the almost constant XMn as well as the increase of Fe# from core towards the rim strongly suggest that the original zoning has been modified by diffusion (*e.g.* Spear, 1993; Groppo *et al.*, , Indares *et al.*,). Two types of feldspars occur in the rock (Fig. 5b). Plagioclase shows XAb between 0.65 and 0.82, with the lowest values found in plagioclase inclusions in garnet (Table 2). Sporadically, almost pure albite (XAb = 0.95-0.96) is found at the edge of matrix plagioclase. K-feldspar is characterized by XOr (= K/(K+Na+Ca)) in the range of 0.86-0.92. Biotite is chemically heterogeneous (Fig. 5c; Table 3). Matrix biotite has Ti a.p.f.u. values between 0.11 and 0.27 with XMg of 0.36-0.39. Biotite inclusions in the garnet rim show the highest XMg (0.53-0.54) with Ti a.p.f.u. = 0.23, whereas late biotite texturally associated with sillimanite, both replacing garnet, is characterized by the lowest Ti a.p.f.u. (0.06-0.07) and XMg of 0.36-0.37. The late white mica is muscovite (Table 4) with Si a.p.f.u. between 3.03 and 3.10 (Fig. 5d).

ESTIMATION OF PRESSURE (P) – TEMPERATURE (T)

386 ***Methods***

387 The *P-T* histories of selected samples were constrained by modelling using pseudosections.
388 Moreover, where possible, trace-element based thermobarometry was applied such as the Zr-in-
389 rutile thermometer (calibration by Tomkins *et al.,* 2007) and the Y-in-garnet thermometer (Pyle &
390 Spear, 2000).
391 *P-T* pseudosections were constructed with the software PERPLE_X (Connolly, 2005, August 2011
392 version, downloaded from the web site http://www.perplex.ethz.ch/). The internally consistent
393 thermodynamic database for minerals and water (CORK model, Holland & Powell, 1991) given by
394 Holland Powell (1998, with 2002 updates) was used. The following solid-solution (a-X)
395 models, compatible with this data set and based on formulations of Holland Powell (1996,
396 1998) and Powell Holland (1999), were chosen: GlTsTsPg for amphibole, T for talc, Ctd(HP)
397 for chloritoid, TiBio(HP) for biotite, Chl(HP) for chlorite, hCrd for cordierite, Gt(HP) for garnet,
398 Opx(HP) for orthopyroxene, Omph(HP) for clinopyroxene, IlGkPy for ilmenite (ideal ilmenite-
399 geikielite-pyrophanite solid solution), Pheng(HP) for potassic white mica (with a maximum
400 paragonite content of 50% mol), St(HP) for staurolite. The models used for feldspars (plagioclase
401 and K-feldspar) and Na-Ca rich mica were reported by Massonne (2012 and references therein).
402 Moreover, for calculating melting relationships within the GHS_U, the model melt(HP) for
403 haplogranitic melt (White *et al.*, 2001) was selected.
404 Calculations were performed in the MnO-Na_2O-CaO-K_2O-FeO-MgO-Al_2O_3-SiO_2-H_2O-TiO_2 model
405 system (MnNCKFMASHT). No ferric iron (or O_2) was considered because: i) magnetite is absent
406 in the selected samples (White et al., 2000); ii) the amount of ferric iron in the minerals is very low
407 and iii) rutile+ilmenite (± graphite) indicate low oxidation conditions (White , 2000; Diener &
408 Powell, Groppo *et al.*, Titanium was included to determine the *P-T* relations of Ti-rich
409 phases. However it must be stressed that the presence of ferric iron would affect their *P-T* relations.
410 The calculated pseudosections were contoured by molar contents of phase components, (*e.g.* pyrope

411 component in garnet) and modal phase amounts. Each raw graph was manually smoothed as shown
412 by Connolly (2005).
413
414 ***Bulk rock composition***
415 The bulk-rock compositions of five selected samples (see above) were determined by X-ray
416 fluorescence (XRF) analysis on ground thin sections chips, following the analytical procedure
417 reported in Massonne (2014). These compositions were simplified in order to fit the ten-component
418 model system: *i*) CaO was reduced applying a correction for phosphorus assumed to be exclusively
419 in apatite; *ii*) various amounts of H_2O were considered in the pseudosection calculations as outlined
420 below.
421 In all calculations for LHS and GHS_L rocks H_2O saturation was permitted in the whole *P-T* range
422 considered. Sample D09-52 (GHS_U) was assumed to be H_2O saturated after cooling below the
423 solidus (*e.g.* Massonne, 2014). As the high grade "peak" assemblage M1 (see above) was preserved
424 in sample D13-28 and showed only minor retrogression, this rock is compatible with a scenario
425 where melt, produced during prograde and peak metamorphism, was partially lost. Therefore, the
426 amount of H_2O was estimated following the method of Hasalová *et al.* (2008) (see also Tajčmanová
427 *et al.*, 2011). Thus, T-XH_2O pseudosections at different constant pressure (1.0, 0.80, 0.70, 0.55
428 GPa) were constructed. The "best fit" water amount *sensu* Hasalová *et al.* (2008) was chosen for
429 calculating the pseudosection for sample D13-28 (see Fig. S6). This pseudosection is, however,
430 valid only for "near peak conditions" to an early retrograde stage (Groppo *et al.*, 2012;
431 Hasalová *et al.*,).
432 Pseudosection modeling requires the crucial identification of the "true" reactive equilibrium volume
433 (effective bulk composition, EBC, Stüwe, 1997), which could change during the metamorphic
434 evolution, for example, by sequestering elements such as Mn in the interior of garnet and
435 subsequent shielding by outer garnet domains. Various methods have been proposed (*e.g.* Stüwe,
436 1997; Evans, 2004) to account for this effect. In our study, garnet with strong growth zoning is

present (see Fig. 4), thus the method proposed by Evans (2004) and Gaides *et al.* (2006) (see also Groppo *et al.*, 2009) to samples D13-75 and D09-10 was applied. In this method garnet considered to be concentrically zoned with different (at least two) shells. A Rayleigh fractionation model for the garnet zoning is assumed, where Mn content is a function of the modal amount of garnet and a curvilinear relationship between Mn and Fe, Mg, Ca contents is present (see Evans, 2004 and references therein). Mineral mode *vs* composition curves for garnet are build up and after integration, it is possible to calculate the composition of a garnet shell that must be subtracted from the whole rock compositions in order to obtain the new EBC.

This approach to sample D13-75 with <5 vol.% of garnet results in a minor effect (see also Groppo *et al.,* 2009; Massonne, 2014), whereas a considerable effect on D09-10, with high modal amount (~ 10 vol.%) and strongly zoned garnet, was noted. In fact, relevant mineral-in curves (except garnet-in) are only slightly shifted, but the *P-T* positions of garnet compositional isopleths are significantly displaced (see below and compares Fig. S3 with Fig. S4).

P-T RESULTS AND PATHS

P-T results obtained with pseudosection modeling are presented below. For each sample only relevant graphs/isopleths are shown. The full sets of contoured graphs are reported in the appendix (Figs S1-S7).

Sample D13-75 (LHS: Grt I zone)

Pseudosection topology

The *P-T* pseudosection for sample D13-75 (Fig. 8a) was calculated for the *P-T* range of 0.1–1.1 GPa and 400–650°C. Quartz is always present in the considered *P-T* range. Garnet appears somewhat below 500°C at < 0.55 GPa. Staurolite occurs in the MT-HT range of the pseudosection, where, at low pressure, also cordierite appears. In the HP-LT range plagioclase is absent, and clinopyroxene (< 2 vol.%) occurs at < 475°C (Fig. 8a).

463

464 *Metamorphic conditions and P-T-D path*

465 The observed assemblage of sample D13-75 (see above) is represented (Fig. 8a) in the field Chl-
466 Wm-Pl-Ilm-Grt-Bt-Qz (+V), which appears between 480-580°C and 0.10-0.80 GPa. This field is
467 limited by the staurolite-in curve (Figs 8a,b) towards high temperatures. Rutile-in and Ca-Na white
468 mica-in curves define the upper pressure limit.
469 The isopleths for the garnet core (XCa~0.19-0.18, XMg~0.03, XFe=0.62) intersect at ~ 525°C and
470 0.55 GPa and, thus, nearly 25 °C above the garnet-in curve (Fig. 8b), in the Chl-Wm-Pl-Ilm-Grt-Bt-
471 Qz field (Fig. 8a) compatible with inclusions of biotite-plagioclase-quartz-ilmenite-chlorite-white
472 mica in this core. The isopleths for the garnet rim (XCa~0.18; XMg~0.07, XFe=0.72) intersect at
473 about 560 °C and 0.75 GPa (Fig. 8b). This intersection is compatible with Si contents of potassic
474 white mica (3.12–3.15 a.p.f.u.) and XMg=0.46–0.45 and 0.48-0.46 of chlorite and biotite (Fig. 8b),
475 respectively, which grew along $S_{P(LHS)}$ (Fig. 6c; Table 1). In summary, LHS sample D13-75 records
476 a *P-T* path (Fig. 8b) characterized by burial and heating. Moreover, since no staurolite is present in
477 the sample, decompression of the LHS sample D13-75 occurred without appreciable heating. In this
478 way, a nearly "hairpin type" *P-T* path is the most probable one experienced by the LHS rocks in the
479 Mugu Karnali area.

480

481 **Sample D13-06 (GHS_L: Grt II zone)**

482 *Pseudosection topology*

483 Sample D13-06 was modeled for the *P-T* range of 0.2–1.2 GPa and 400–700°C (Fig. 8c). Quartz is
484 present in all fields, whereas clinopyroxene (< 5.5 vol%) and titanite appear only at LT-HP
485 conditions of the pseudosection. Garnet occurs at almost the entire P-T conditions except in the LT-
486 LP and LP-HT portions of the pseudosection (Fig. 8c).

487

488 *Metamorphic conditions and P-T-D path*

The isopleths of garnet with the highest XMg=0.69 (XCa=0.15, XFe=0.75, XMn=0.03) intersect in the *P-T* range of ~ 1.0-1.2 GPa and 600°C (Fig. 8d) in the Wm-Pl-Ilm-Grt-Pg-Bt-Qz-V field, compatible with the observed mineral assemblage (see above), although the predicted Na-Ca white mica was not found. Several reasons such as: (i) paragonitic mica was completely exhausted during retrogression; (ii) this mica occurs only in submicroscopic interlayers in potassic white mica (*e.g.* Willner *et al.*, 2009); or (iii) possible flaws in mica solution models (*e.g.* Groppo *et al.*, 2009) could be responsible for that. However, the *P-T* conditions of ~ 1.0-1.2 GPa and 600°C are in agreement with the highest Si content in white mica (3.25 a.p.f.u.). An intersection of isopleths for the garnet outer rim (XMg~0.06, XCa=0.13-0.12, XFe~0.17, XMn~0.07) occurs at *P-T* conditions of ~ 0.8 GPa and 570°C, along the retrograde path, where garnet is consumed and re-equilibrated. Further decompression and cooling is suggested by the lowest Si content in white mica (3.10-3.09 a.p.f.u.) and by XMg in biotite (0.37-0.35). According to the pseudosection, the late chlorite after garnet formed below 520°C. Thus, the D13-06 sample records only a small part of the experienced *P-T* path (Fig. 8d).

Sample D09-10 (GHS_L: St + Bt ± Ky zone)

Pseudosection topology

The *P-T* pseudosection for sample D09-10 was calculated for the range of 0.3–1.3 GPa and 400–700°C (Fig. 9a). The garnet-in curve is located in the pressure range of 0.3–0.7 GPa at ~ 520°C (Fig. 9a) and, thus ~ 15-20°C above the biotite-in curve (field n°13 in Fig. 9a). Chlorite is completely consumed around 580°C in almost the entire pressure range (Fig. 9a). Aluminosilicate (kyanite or sillimanite) occurs in the HT range of the pseudosection (Fig. 9a). In the LT-HP corner of the pseudosection lawsonite appears. Staurolite occurs in a narrow field from ~ 535°C (at 0.30 GPa) up to 650-670°C (at 0.75–0.85 GPa).

Metamorphic conditions and P-T-D path

The observed mineral assemblage (see above) is restricted to a small field at 0.75–0.85 GPa and 640–660°C (labeled as Grt-Wm-Bt-St-Ky-Qz-Pl-Ilm in Fig. 9a). This field is also present, but somewhat shifted to slightly higher temperatures (660-680°C) in the garnet core fractionated bulk composition (Figs 9b & S4). A *P-T* path (Fig. 9a) is reconstructed using mineral associations and their compositions. According to compositional isopleths (XMg=0.03, XCa=0.18, XFe=0.66, XMn~0.13-0.12), the garnet core formed at ~ 520°C and 0.60 GPa, very close to the garnet-in curve (Fig. 9b). This temperature is further supported (Fig. 9b) by the applied garnet-xenotime thermometry. This thermometry is applicable since xenotime was observed in the garnet core, buffering its YAG content (Y in garnet core = 1800–900 ppm). Moreover, these *P-T* values are compatible with the presence of chlorite-biotite-ilmenite and Na-Ca white mica in the garnet core in agreement to the calculated field in the pseudosection. Garnet mantle compositional isopleths (XMg=0.12-0.11, XCa=0.06-0.05, XFe=0.81, XMn=0.004-0.005) do not perfectly intersect, but suggest an equilibration of this garnet domain around 580–600°C and 1.1 GPa. This high-pressure stage is compatible with highest Si content in white mica (3.21 a.p.f.u.) and would explain the rutile relicts observed in the rock. Finally, the garnet outermost rim (XMg=0.15–0.14, XCa=0.05-0.04, XFe=0.80-0.81, XMn=0.008-0.01), joined with the compositions (Table 4) of white mica (3.09-3.11 a.p.f.u.) and biotite (XMg=0.45–0.50) defining $S_{(PGHS)}$, and staurolite (XMg= 0.18–0.16) equilibrated at ~ 650–670°C and 0.80–0.85 GPa (Fig. 9b). These conditions are compatible with the narrow *P-T* range of the observed mineral assemblage (Grt-Wm-Bt-St-Ky-Qz-Pl-Ilm in Fig. 9a). In summary, sample D09-10 from the GHS_L has experienced a "clockwise type" *P-T* path (Fig. 9b) with peak pressure (P_{max}) conditions of 1.1 GPa at 580–600°C reached before the maximum temperature (T_{max}, see also Rolfo et al., 2015) of 650–670°C (0.80–0.85 GPa) at which the Barrovian minerals kyanite and staurolite are predicted to have been grown. Further decompression accompanied by cooling is inferred based on the lack of sillimanite, white mica formed after kyanite, and the formation of retrograde chlorite.

Sample D09-52 (GHS_U: Als + Wm zone)

Pseudosection topology

The *P-T* pseudosection for sample D09–52 (Fig. 9c) was calculated for the range ~~of~~ 0.3–1.3 GPa and 575–800°C. Quartz is stable in the whole *P-T* pseudosection as garnet except at very LP (< 0.45 GPa) and MT (< 680 °C). Biotite is absent at LP-HT conditions (above field n°16 in Fig. 9c) due to the formation of cordierite (+K-feldspar). White mica is limited towards high temperature by partial melting reactions leading to the formation of K-feldspar + aluminosilicate (*e.g.* fields 17 & 25 in Fig. 9c). Melt is predicted to appear already at MT and HP conditions (600–620°C and 1.2–1.3 GPa). It should be kept in mind that these melting conditions are related to minimum melting, assuming a wet-solidus environment (*i.e.* the rock contains free H_2O). Lower H_2O contents can shift the solidus towards higher T (Massonne, 2014; Weinberg & Hasalová, 2015). At temperatures slightly exceeding the wet-solidus, very little melt will be produced and is, thus, difficult to detect (White *et al.,* 2001). Taking into account these limitations (see also Massonne, 2014) it is possible to derive a path for this sample (Fig. 9d).

Metamorphic conditions and P-T-D path

Garnet rim isopleths (XMg=0.15-0.12, XCa=0.05-0.03, XFe=0.79–0.78, XMn=0.02-0.12), despite the low intersection angle (*i.e.* larger uncertainties), define *P-T* conditions of ~ 0.7–0.8 GPa and 690–710°C compatible with the preserved assemblage (Sil-Grt-Wm-Bt-Pl-Qz-Ilm), which was calculated to coexist with few vol.% melt. These conditions are also compatible with the chemistry of syn-kinematic white mica (Si a.p.f.u.=3.12–3.10) and biotite (XMg=0.47–0.55). A higher *P*, pre-mylonitic, stage is suggested by the composition of the cores of large white mica fishes. This HP stage is tentatively placed at around 1.2 GPa and 630–650°C using the chemistry of cores of white mica fishes (XMg =0.48–0.52 and Si a.p.f.u. = 3.25) and XCa (0.10) and XMg (0.10-0.09) in some garnet cores.

Hence, sample D09-52 experienced a clockwise *P-T* path from HP conditions of ~1.2 GPa and 630–650°C up to MP-HT conditions of 0.7–0.8 GPa and 690–720 °C, at possible supra-solidus conditions (Fig. 9d). The lack of staurolite and K-feldspar indicates further decompression accompanied by cooling. This *P-T* path is compatible with syn-kinematic growth of sillimanite along the mylonitic foliation $S_{P(GHS)}$ and rutile relicts observed within garnet, in the large white mica porphyroclasts and in the matrix ilmenite. Moreover, this path could also account for kyanite relicts observed in other samples from the same outcrop.

Sample D13-28 (GHS_U: Als + Kfs zone)

Pseudosection topology

D13-28 has been modeled using a *P-T* pseudosection for 0.3–1.3 GPa and 650–900°C (Fig. 10a). The H_2O in the calculation was estimated to be 0.20 wt% (see "bulk rock composition" section), but this amount could be to too low (*e.g.* Iaccarino *et al.*, Braga & Massonne,), as lower water contents do not stabilize white mica during cooling. However, higher H_2O contents destabilize aluminosilicate (Fig. S6). Moreover, the estimated 0.2 wt% H_2O is well within the range of estimates for high-grade migmatites (Hasalová *et al.*, 2008; Groppo *et al.,* 2010, 2012; Tajčmanová *et al.*, 2011). Quartz, plagioclase and K-feldspar are always present in the considered *P-T* space, and also garnet, except in the HT-LP range, where firstly cordierite and then orthopyroxene appear with rising temperature. Biotite is completely consumed at ~ 800°C (Figs 10a,b). Kyanite occurs above 725°C and 0.9 GPa in the pseudosection. White mica occupies the LT-HP side of the graph (650–800°C, 0.6–1.3 GPa). Melt appears around 700–725°C as a function of P (Figs 10a,b). Rutile occurs above 0.8–0.9 GPa, whereas ilmenite is present below these pressures (Figs 10a,b).

Metamorphic conditions and P-T-D path

591 The peak conditions of around 1.0-1.1 GPa and ~ 740–775°C (Fig. 10a) are constrained by the M1
592 assemblage (see above) Grt-Ky-Kfs-Pl-Qz-Bt-Rt-L which is typical for the HP granulite facies (*e.g.*
593 Indares *et al.*, 2008; Groppo *et al.*, 2010; 2012). The *P-T* field of this assemblage field is delimited
594 towards lower T and P by the disappearance of kyanite, and towards higher T by the Bt-out curve
595 (Figs 10a,b). These HT conditions (~ 700 up to 750 °C) are further supported by Zr-in-rutile
596 thermometry (Zr = 540–800 ppm) applying the Tomkins *et al.* (2007) calibration (Fig. 10b) on
597 pristine rutile lacking ilmenite retrogression and/or zircon exsolution (see Fig. S8).
598 The M2 paragenesis (Grt-Sil-Kfs-Pl-Qz-Bt-Ilm±Wm/melt) appears below 0.85 GPa. At
599 temperatures above 700–725°C melt occurs, whereas at lower temperature white mica joins the
600 assemblage. Using such constraints, sample D13-28 records a segment of a "clockwise" *P-T* path
601 characterized by decompression and cooling (Fig. 10b) from conditions of ~ 750°C, ≥1.0 GPa to
602 0.80–0.70 GPa and ~ 700°C. In the proposed *P-T* segment garnet and melt are consumed via back-
603 reactions such as Grt+Kfs+L = Sil+Bt (+Wm) (*e.g.* Spear *et al.,* 1999; Groppo *et al.*, 2012). This *P-*
604 *T* path (Fig. 10b) is compatible with compositional isopleths of biotite XMg (0.54-0.40) and garnet
605 (XFe = 0.69-0.71 for the inner rim, XFe = 0.76 for the outer rim), as well as the late white mica
606 chemistry. However, in the M1 field of the calculated pseudosection, the calcium isopleths for
607 garnet do not exactly match the derived *P-T* conditions. Intersections of rim isopleths (XCa>0.05)
608 suggest higher pressure conditions (1.20–1.40 GPa) above the M1 field. This is a frequent
609 observation in HP migmatites (*e.g.* Indares *et al.*, 2008) also in the Himalaya (Groppo *et al.*, 2010,
610 2012) and it is probably related to the presence of another Ca-bearing phase in the system, such as
611 apatite (Indares *et al.*, 2008; Groppo *et al.*, 2012) which in D13-28 is present as large grains and in
612 appreciable modal amounts, but not modeled in the pseudosection. Indares *et al.* (2008)
613 hypothesized that the incorporation of Ca in the melt at high pressures, is not favored and garnet
614 would incorporate Ca released during apatite dissolution. Modal changes of apatite could result in
615 the depletion or enrichment of the bulk Ca and so zoning of XCa in garnet from anatectic apatite-
616 bearing pelitic systems may not always be a reliable indicator of the *P–T* (Indares *et al.*, 2008;

Groppo *et al.*, 2012). For these reasons, it is stressed that the obtained "peak" *P-T* conditions are believed as minimum one (*e.g.* Guilmette *et al.*, 2011; Groppo *et al.*, 2010; 2012). Despite these limitations, the proposed *P-T* path could explain textural key observations, such as: (i) the peritectic origin of garnet, suggested by K-feldspar inclusions; (ii) syn-kinematic replacement of kyanite by sillimanite; (iii) replacement of garnet edges by sillimanite+biotite; (iv) replacement of rutile by ilmenite coronae in the matrix; (v) the late growth of white mica flakes (*e.g.* Brown, 2002). Moreover, these observations support the shearing activity of the TSZ at high temperature conditions, as also suggested by quartz and feldspar microstructures (see above).

DISCUSSION

Structural architecture

The Himalayan portion investigated in this work is characterized by a structural regional architecture that could be approximated to a NE-E dipping homoclinal slab (Fig. 2). Despite this apparent regional structural simplicity, a protracted deformational history has been highlighted. Several high-strain zones, at different structural positions, with non-coaxial deformation, have been developed (Figs 1c, 2). The lowest one, mapped as the MCTZ, juxtaposed middle- to high-grade GHS rocks structurally above the medium- to low- grade LHS.

Within the GHS, two high-grade shear zones have been mapped (Figs 1c, 2). The lower one, the MSZ described by Montomoli *et al.* (2013), juxtaposed the sillimanite-bearing GHS_U on the GHS_L in the time span of *c.* 25–18 Ma (Montomoli *et al.*, 2013).

The structurally upper TSZ is located at a higher structural level within the GHS_U and coincides with the prograde white mica disappearance and aluminosilicate + K-feldspar + melt appearance. The TSZ hanging-wall is made of a migmatitic complex (stromatites and minor diatexites) and by the Mugu granite (Fig. 1c). No geochronological data are available for the TSZ, but at least from the structural point of view, the TSZ could be compared with the Kalopani Shear Zone in the

642 nearby Annapurna area (Vannay & Hodges, 1996; Carosi *et al.*, 2014, 2016) or with the "Thrust 3"
643 of He *et al.* (2015).
644 Barrovian minerals show complex relationships with the deformation and time of crystallization.
645 For instance, within the LHS (sample D13-75) garnet is early-syn- to syn-kinematic with respect to
646 the main foliation ($S_{P(LHS)}$), and, going progressively structurally upward in the GHS_L, garnet (in
647 Grt II zone), staurolite and potentially kyanite appear as early-syn to syn-kinematic minerals with
648 respect to the development of $S_{P(GHS)}$ (see also Yakymchuk & Godin, 2012). In the GHS_U garnet
649 and kyanite (± K-feldspar) are pre-kinematic, whereas sillimanite is syn-kinematic with respect to
650 the development $S_{P(GHS)}$. These microstructural observations support a diachronous mineral growth
651 and rock equilibration/deformation across the Mugu Karnali transect. This picture, as proposed
652 here, is different from that one suggested by Stephenson *et al.* (2000). These authors interpreted
653 staurolite and kyanite mainly as early minerals, occurring during the first stages of metamorphism
654 (M1) and predating the development of $S_{P(GHS)}$, and K-feldspar as a late mineral related to the
655 subsequent stage (M2).
656 Finally it is worthy of note that when the tectonic units experienced a late folding event followed by
657 brittle tectonics when they reached upper structural levels.
658
659 *Metamorphism and P-T path*
660 Pseudosections were used to constrain the *P-T* history of the metamorphic core of the Mugu Karnali
661 transect (Fig. 11). The present estimates are compatible, within the methodological errors, with
662 THERMOCALC average *P-T* results obtained on a larger sample dataset, including samples
663 investigated in the present contribution, reported in Iaccarino (2015). Moreover, for samples D09-
664 10 and D09-52, the present findings are also compatible with *P-T* estimates based on "classical
665 geothermobarometry" reported in Montomoli *et al.* (2013). Results obtained in the present
666 contribution could be compared with THERMOCALC average *P-T* estimates of Yakymchuk &
667 Godin (2012) for a nearby structural profile, where very similar *P-T* conditions were obtained

668 especially for the GHS_L. Lower *P-T* conditions are reported by these authors for the aluminosilicate
669 + K-feldspar zone within the GHS_U, although Yakymchuk & Godin (2012) argued that their results
670 are better interpreted as partial re-equilibration somewhere along a decompression path. This would
671 be compatible with our findings.
672 Different *P-T* paths were inferred from the studied samples (Fig. 11) and the following results could
673 be traced and compared with other structural transects along the belt:
674 (i) The LHS (sample D13-75) is characterized by a "hairpin type" *P-T* path (with T_{max} being nearly
675 coincident with peak P_{max}), as already noted for other portions of the Himalaya (*e.g.* Kohn, 2014
676 and references therein). This *P-T* path type seems to be common for MCTZ footwall rocks (*e.g.*
677 Kohn *et al.*, 2001; Groppo *et al.,* 2009; Rolfo *et al.*, 2015).
678 (ii) GHS samples have likely experienced a *P-T* path with a steep dP/dT before reaching P_{max},
679 followed by decompression associated with heating from P_{max} up to T_{max} (*e.g.* Groppo *et al.*, 2009,
680 2010, 2012; Rolfo *et al.*, 2015) and further decompression and cooling.
681 (iii) GHS_U samples have experienced HP conditions (D09-52; D13-28) ~~well~~ comparable, but not
682 necessarily coeval with GHS_L rocks (samples D13-06; D09-10). These HP conditions were largely
683 overprinted by sillimanite-bearing assemblages (*e.g.* Groppo *et al.,* 2009, 2010, 2012; Rolfo *et al.*,
684 2015). Nevertheless, according to our experience, garnet compositions and their evaluation with *P-*
685 *T* pseudosections have the capability to "detect" such a former HP metamorphic stage within the
686 GHS_U migmatites (*e.g.* Groppo *et al.*, 2010, 2012). Interestingly, at HP conditions, melt was already
687 present in the rock. With respect to this point, it must be stressed that melting during isothermal
688 decompression (Harris & Massey, 1994) is efficient if white mica is present at HP conditions (*e.g.*
689 Guilmette *et al.*, 2011; Groppo *et al.*, 2012), otherwise, if this mineral is consumed along the
690 prograde heating, on decompression its role is rather minor, since the path is nearly parallel to the
691 melt isomodes (*e.g.* Guilmette *et al.*, 2011; Groppo *et al.*, 2012). This aspect could have a deep
692 impact on migmatite rheology and on exhumation process (*e.g.* Groppo *et al.*, 2012; Yakymchuk &
693 Brown, 2014). Indeed, coupled with the melt extraction and the following upward displacement of

the migmatite solidus (Yakymchuk & Brown, 2014), an increase of rock viscosity and a shifting from diffuse to localized deformation would be possible.

Finally, it is worthy of note that the present *P-T* results along the Mugu Karnali transect are in agreement with both absolute values and shapes of *P-T* paths obtained by Groppo *et al.* (2009) for the metamorphic core in Eastern Nepal (see the review of Rolfo *et al.*, 2015).

P-T-d-t and tectonic implications

P-T arrays are often used to constrain exhumation models of the GHS and of the Himalayan tectonics. *P-T* profiles are compared (*e.g.* Kohn, 2008, 2014; Groppo *et al.*, 2012; Yakymchuk & Godin, 2012; Rolfo *et al.*, 2015;) with the *P-T* paths predicted by numerical or thermo-mechanical models (*e.g.* channel flow model, Jamieson *et al.*, 2004, 2006 or critical taper model, Kohn, 2008 and references therein).

The LHS "hairpin" *P-T* path (D13-75) is in agreement with a critical taper model. GHS paths, characterized by decompressional heating, could be more compatible with a channel flow model (*e.g.* Kohn, 2014). Indeed, *P-T* paths for a LHS channel flow should be clockwise (*e.g.* Caddick *et al.*, 2007; Caddick & Kohn, 2013), whereas GHS paths in the critical taper model lack heating during decompression (Kohn, 2008). However, Gervais & Brown (2011) pointed out that neither a *P-T* path alone nor the absolute *P-T* peak is diagnostic for exhumation models. Instead, their timing associated with the strain path could be diagnostic. If we take into account the available geochronological data in the study area, the following time constraints are possible: (i) Carosi *et al.* (2013) demonstrated that the STDS shearing in Western Nepal was active before *c.* 24 Ma; (ii) Montomoli *et al.* (2013) pointed to an exhumation of the GHS_U, related to the activity of the MSZ, between 25–18 Ma, while the GHS_L was still experiencing an underthrusting stage; (iii) GHS_L prograde monazite ages are as young as 17 Ma, whereas retrograde ages (likely related to the MCTZ activity), as young as 13 Ma, are reported (Montomoli *et al.,* 2013); (iv) Robinson *et al.* (2006) provided white mica Ar-Ar (cooling) ages for the GHS (GHS_U in Yakymchuk & Godin,

720 2012), located west of the Mugu Karnali valley, as old as 25 Ma; (vi) Gibson *et al.* (2016), for
721 samples located south of the here investigated area, reported white mica Ar-Ar cooling ages of *c.* 14
722 Ma for GHS_U, and *c.* 19 Ma, interpreted as deformation ages, for GHS_L samples.
723 These data, at least in Western Nepal, point to (i) a short duration of coeval activity of the STDS
724 with basal thrusting (likely along the MSZ); and (ii) an activity of the MCTZ that lasted longer than
725 that one of the STDS. Cooling/retrograde ages obtained from rocks of the GHS_U of this region
726 overlap with prograde ages of the GHS_L. Systematic rejuvenation of metamorphic ages (both
727 prograde and retrograde) going structurally downward has been frequently observed for the GHS
728 (*e.g.* Kohn *et al.*, 2001; Corrie & Kohn, 2011; Larson *et al.,* 2013; Kohn, 2014, 2016; Wang *et al.*,
729 2015; Carosi *et al.,* 2016). These ages could testify a diachronic equilibration controlled by the
730 structural position in the GHS.
731 The presented observations (porphyroblast-matrix relationship, different *P-T* paths and their timing)
732 do not favour the nearly flat pre-MCT isograds as proposed in the model of isograd-folding
733 (Stephenson *et al.*, 2001; Searle & Szulc, 2005), a post-metamorphic shearing of isograds (*e.g.*
734 Hubbard, 1996), or an inverted temperature gradient through conductive heating (hot iron effect of
735 Le Fort, 1975). Instead, a complex interaction of progressive deformation and metamorphism (see
736 also Cottle *et al.*, 2015) is proposed for the assembly of the GHS, and the HMC in general, where
737 different tectonic slices from below (Indian Plate) are accreted at greater depths tectonically
738 juxtaposing slices with a diachronic metamorphic and deformational history. The MSZ, and perhaps
739 the TSZ as well, represent tectonic boundaries of these slices. The process of fast exhumation of
740 thin crustal slices has been recently invoked by Spear (2014) in order to explain his garnet diffusion
741 profile models for the Devonian Acadian metamorphic event in Vermont. Exhumation of high-
742 grade rocks due to thrusting alone has been shown elsewhere (Platt, 1993; Ring *et al.*, Stüwe
743 & Barr, to be ineffective. Thus, a combination of thrusting plus erosion (starting in the
744 Himalaya during the Eocene *e.g.* Najman *et al.,* 2008, Carosi *et al.,* 2016), and/or thrusting plus
745 ductile thinning (Ring *et al.,* 1999), and/or thrusting plus normal faulting is required. During this

746 exhumation stage the STDS could be active or inactive, in alternating periods of coeval activity
747 (*e.g.* Chambers *et al.*, 2011) with basal thrusting.
748 In the light of our new findings, it appears that an updated tectonic model, which could account for
749 all structural complexities, is needed for the Himalaya (*e.g.* Cottle *et al.*, 2015). However, as
750 already proposed in Fraser *et al.* (2000), one point should be considered: "models based on the
751 preserved metamorphic field gradient, and that consider the HHC [*i.e.* GHS] as a single coherent
752 section, must be considered suspect" (Fraser *et al.,* 2000).
753 According to the presented P-T-d-t paths of the HMC, a kinematic model where the HMC is
754 progressively build up and exhumed by in-sequence shearing (*e.g.* Carosi *et al.,* 2016) is favoured.
755 Ductile thinning of the HMC and normal faulting (along the STDS) would assist the exhumation
756 process.
757 Finally, caution is strongly recommended in assuming that the tectono-metamorphic history of the
758 low-grade part of metamorphic terranes (*e.g.* GHS_L) could be the same of that registered by higher-
759 grade samples (*e.g.* GHS_U, see also Spear & Rumble, 1986). Available geochronological data in the
760 GHS (*e.g.* Corrie & Kohn, 2011; Larson *et al.,* 2013; Montomoli *et al.,* 2013; Kohn, 2014, 2016;
761 Wang *et al.,* 2015) often show that both prograde and retrograde metamorphic ages, are younger in
762 the lower grade metamorphic rocks respect to the higher grade, that is the opposite of what could be
763 expected for a "simple" prograde path (*e.g.* Weller *et al.*, 2013).
764

765 **ACKNOWLEDGEMENTS**

766 The authors are grateful to T. Theye (Universität Stuttgart) for the help with the EMP work
767 performed at Institut für Mineralogie und Kristallchemie (Universität Stuttgart). Research was
768 supported by PRIN 2010–2011 (to Carosi R. and Montomoli C.), by PRA 2016 (to Montomoli C.)
769 and by the University of Padova (to Visonà D.). C. Yakymchuk and A. Indares are thanked for their
770 constructive and thorough reviews, which improved the quality of the manuscript. We appreciate
771 the suggestions and editorial handling by D. Robinson.

REFERENCES

Arita, K., Shiraisci, K. & Doigoro, H., 1984. Geology of Western Nepal and a comparison with Kumaun, India. *Journal of the Faculty of Science, Hokkaido University, Series IV*, **21**, 1–20.

Bartoli, O., Acosta-Vigil, A., Ferrero, S. & Cesare, B., 2016. Granitoid magmas preserved as melt inclusions in high-grade metamorphic rocks. *American Mineralogist,* **101,** 1543–1559.

Bertoldi, L., Massironi, M., Visonà, D., Carosi, R., Montomoli, C., Gubert, F., Naletto G. & Pelizzo, M.G., 2011. Mapping the Buraburi granite in the Himalaya of Western Nepal: remote sensing analysis in a collisional belt with vegetation cover and extreme variation of topography. *Remote Sensing of Environment*, **115,** 1129–1144.

Braga, R. & Massonne, H.-J., 2012. H_2O content of deep-seated orogenic continental crust: the Ulten Zone, Italian Alps. *International Geology Review,* **54,** 633–641.

Brandelik, A. 2009., CALCMIN–an EXCEL^{TM} Visual Basic application for calculating mineral structural formulae from electron microprobe analyses source. *Computers and Geosciences,* **35,** 1540-1551.

Brown, M., 2002. Retrograde processes in migmatites and granulites revisited. *Journal of Metamorphic Geology*, **20,** 25–40.

Burg, J.P., Brunel, M., Gapais, D., Chen, G.M. & Liu, G.H., 1984. Deformation of leucogranites of the crystalline Main Central Sheet in southern Tibet (China). *Journal of Structural Geology*, **6,** 535–542.

Caddick, M.J. & Kohn, M.J., 2013. Garnet: Witness to the evolution of destructive plate boundaries. *Elements*, **9,** 427–432.

794 Caddick, M.J., BIckle, M.J., Harris, N.B.W., Holland, T.J.B., Horstwood, M.S.A., Parrish, R.R. &
795 Ahmad, T., 2007. Burial and exhumation history of a Lesser Himalayan schist: Recording the
796 formation of an inverted metamorphic sequence in NW India. *Earth and Planetary Science Letters*,
797 **264,** 375–390.

798 Carosi, R., Montomoli, C., Rubatto, D. & Visonà D., 2010. Late-Oligocene high temperature shear
799 zones in the core of the Higher Himalayan Crystallines (Lower Dolpo, Western Nepal). *Tectonics*,
800 **29**.

801 Carosi, R., Montomoli, C., Iaccarino, S., Massonne, H.-J., Rubatto, D., Langone, A., Gemignani, L.
802 & Visonà D., 2016. Middle to late Eocene exhumation of the Greater Himalayan Sequence in the
803 Central Himalayas: progressive accretion from the Indian plate. *The Geological Society of America*
804 *Bulletin*, doi:10.1130/B31471.1.

805 Carosi, R., Montomoli C., Rubatto, D. & Visonà D., 2013. Leucogranite intruding the South
806 Tibetan Detachment in western Nepal: implications for exhumation models in the Himalayas. *Terra*
807 *Nova*, **25,** 478–489.

808 Carosi, R., Montomoli, C. &Visonà, D., 2002. Is there any detachment in the Lower Dolpo (western
809 Nepal)? *Comptes Rendus Geoscience*, **334,** 933–940.

810 Carosi, R., Montomoli, C. & Visonà, D., 2007. A structural transect in the Lower Dolpo: insights
811 on the tectonic evolution of Western Nepal. *Journal of Asian Earth Sciences*, **29,** 407–423.

812 Chambers, J., Parrish, R., Argles, T., Harris, N. & Horstwood, M., 2011. A short-duration pulse of
813 ductile normal shear on the outer South Tibetan detachment in Bhutan: alternating channel flow and
814 critical taper mechanics of the eastern Himalaya. *Tectonics*, **3,** TC2005. doi:
815 10.1029/2010TC002784.

816 Connolly, J.A.D., 2005. Computation of phase equilibria by linear programming: A tool for
817 geodynamic modeling and its application to subduction zone decarbonation. *Earth and Planetary*
818 *Science Letters*, **236,** 524–541.

819 Corrie, S.L. & Kohn, M.J., 2011. Metamorphic history of the Central Himalaya, Annapurna region,
820 Nepal, and implication for tectonic models. *Geological Society of American Bulletin*, **123,** 1863–
821 1879.

822 Cottle, J.M., Larson K.P. & Kellett D.A., 2015. How does the mid-crust accommodate deformation
823 in large, hot collisional orogens? A review of recent research in the Himalayan orogen. *Journal of*
824 *Structural Geology,* **78,** 119-133.

825 Diener, J.F.A. & Powell, R., 2010. Influence of ferric iron on the stability of mineral assemblages.
826 *Journal of Metamorphic Geology*, **28,** 599–613.

827 Evans, T.P., 2004. A method for calculating effective bulk composition modification due to crystal
828 fractionation in garnet-bearing schist: implication for isopleth thermobarometry. *Journal of*
829 *Metamorphic Geology,* **22,** 547–557.

830 Fraser, G., Worley, B. & Sandiford, M., 2000. High-precision geothermobarometry across the High
831 Himalayan metamorphic sequences, Langtang valley, Nepal. *Journal of Metamorphic Geology,* **18,**
832 665–685.

833 Fuchs, G., 1974. On the Geology of the Karnali and Dolpo Regions, West Nepal. *Mitteilungen der*
834 *Geologischen Gesellschaft in Wien,* **66-67,** 21–35.

835 Fuchs, G., 1977. The Geology of the Karnali and Dolpo regions, Western Nepal. *Jahrbuch der*
836 *Geologischen Bundesanstalt, Wien,* **120,** 165–217.

837 Gaidies, F., Abart, R., De Capitani, C., Schuster, R., Connolly, J.A.D. & Reusser, E. 2006.
838 Characterization of polymetamorphism in the Austroalpine basement east of the Tauern Window
839 using garnet isopleth thermobarometry. *Journal of Metamorphic Geology,* **24,** 451–475.

840 Garzanti, E., 1999. Stratigraphy and sedimentary history of the Nepal Tethys Himalaya passive
841 margin. *Journal of Asian Earth Sciences,* **17,** 805–827.

842 Gervais, F. & Brown, R.L., 2011. Testing modes of exhumation in collisional orogens:
843 Synconvergent channel flow in the southeastern Canadian Cordillera. *Lithosphere*, **3,** 55–75.

844 Gibson, R., Godin, L., Kellett D.A., Cottle, J.M. & Archibald, D., 2016. Diachronous deformation
845 along the base of the Himalayan metamorphic core, west-central Nepal. *Geological Society of*
846 *America Bulletin,* in press, doi: 10.1130/B31328.1

847 Godin, L., Grujic, D., Law, R.D. & Searle, M.P., 2006. Channel flow, ductile extrusion and
848 exhumation in continental collision zones: an introduction. *Geological Society of London Special*
849 *Publication,* **268,** 1–23.

850 Groppo, C., Rolfo, F. & Lombardo, B., 2009. P–T evolution across the Main Central Thrust Zone
851 (Eastern Nepal): hidden discontinuities revealed by petrology. *Journal of Petrology,* **50,** 1149–
852 1180.

853 Groppo, C., Rubatto, D., Rolfo, F. & Lombardo, B., 2010. Early Oligocene partial melting in the
854 Main Central Thrust Zone (Arun Valley, eastern Nepal Himalaya). *Lithos*, **118,** 287–301.

855 Groppo, C., Rolfo, F. & Indares, A. 2012. Partial Melting in the Higher Himalayan Crystallines of
856 Eastern Nepal: the effect of decompression and implications for the 'Channel Flow' Model. *Journal*
857 *of Petrology,* **53,** 1057–1088.

858 Guilmette, C., Indares, A. & Hébert, R., 2011. High-pressure anatectic paragneisses from the
859 Namche Barwa, Eastern Himalayan Syntaxis: Textural evidence for partial melting, phase equilibria
860 modeling and tectonic implications. *Lithos*, **124,** 66–81.

861 Guillot, S., Cosca, M., Allemand, P. & Le Fort, P., 1999. Contrasting metamorphic and
862 geochronologic evolution along the Himalayan belt. *Geological Society of America, Special Paper,*
863 **328,** 117–128.

864 Hagen, T., 1969. Report on the geological survey of Nepal preliminary reconnaissance. Zürich,
865 *Mémoires de la societe Helvétique des sciences naturelles*, pp. 185.

866 Harrison, T.M., Grove, M., McKeegan, K.D., Coath, C.D., Lovera, O.M. & Le Fort, P., 1999.
867 Origin and episodic emplacement of the Manaslu Intrusive Complex, Central Himalaya. *Journal of*
868 *Petrology,* **40,** 3–19.

869 Harris, N. & Massey, J., 1994. Decompression and anatexis of Himalayan metapelites. *Tectonics*,
870 **13,** 1537–1546.

871 Hasalová, P., Štípská, P., Powell, R., Schulmann, K., Janoušek, V. & Lexa, O., 2008. Transforming
872 mylonitic metagranite by open-system interactions during melt flow. *Journal of Metamorphic*
873 *Geology,* **26,** 55–80.

874 He, D., Webb. A. W., Larson, K.P., Martin, A.J. & Schmitt, A.K., 2015. Extrusion vs. duplexing
875 models of Himalayan mountain building 3: duplexing dominates from the Oligocene to Present.
876 *International Geology Review,* **57,** 1–27.

877 Heim, A. & Gansser, A., 1939. Central Himalaya: geological observations of the Swiss expedition
878 1936. *Memoir Society Helvetica Science Nature,* **73,** 1–245.

879 Hodges, K. V., 2000. Tectonics of Himalaya and southern Tibet from two perspectives. *Geological*
880 *Society of America Bulletin,* **112,** 324–350.

881 Holland, T.J.B. & Powell, R., 1991. A compensated-Redlich-Kwong (CORK) equation for volumes
882 and fugacities of CO_2 and H_2O in the range 1 bar to 50 kbar and 100-1600°C. *Contributions to*
883 *Mineralogy and Petrology,* **109,** 265–273.

884 Holland, T.J.B. & Powell, R., 1996. Thermodynamics of order–disorder in minerals. 2. Symmetric
885 formalism applied to solid solutions. *American Mineralogist*, **81,** 1425–1437.

886 Holland, T.J.B. & Powell, R., 1998. An internally consistent thermodynamic data set for phases of
887 petrological interest. *Journal of Metamorphic Geology,* **16,** 309-343.

888 Hubbard, M.S., 1996. Ductile Shear as a cause of inverted metamorphism: example from the Nepal
889 Himalaya. *The Journal of Geology,* **104,** 493-499.

890 Iaccarino, S., 2015. Tectono-metamorphic evolution of the Greater Himalayan Sequence (GHS) in
891 Western and Central Nepal (Central Himalaya): insights on the exhumation of deep-seated crustal
892 rocks. Unpublished PhD thesis, Pisa, Italy, Università di Pisa, 275 pp.

893 Iaccarino, S., Montomoli, C., Carosi, R., Massonne, H.-J., Langone, A. & Visonà D., 2015,
894 Pressure–temperature–time–deformation path of kyanite-bearing migmatitic paragneiss in the Kali
895 Gandaki valley (Central Nepal): Investigation of Late Eocene–Early Oligocene melting processes.
896 *Lithos*, **231,** 103–121.

897 Imayama, T., Takeshite, T., Yi, K., Cho, D. -L., Kitajima, K., Tsutsumi, Y., Kayama, M., Nishido,
898 H., Okumura, T., Yagi, K., Itaya, T. & Sano, Y., 2012. Two-stage partial melting and contrasting
899 cooling history within the Higher Himalayan Crystalline Sequence in the far-eastern Nepal
900 Himalaya. *Lithos*, **134–135,** 1–22.

901 Indares, A., White, R.W. & Powell, R., 2008. Phase equilibria modelling of kyanite-bearing
902 anatectic paragneiss from the central Grenville Province. *Journal of Metamorphic Geology,* **26,**
903 815–836.

Jamieson, R.A. & Beaumont, C., 2013. On the origin of orogens. *Geological Society of America Bulletin,* **30,** doi: 10.1130/B30855.1

Jamieson, R.A., Beaumont, C., Medvedev, S. & Nguyen, M.H., 2004. Crustal channel flows: 2. Numerical models with implications for metamorphism in the Himalayan-Tibetan orogen. *Journal of Geophysical Research,* **109,** B06407, doi:10.1029/2003JB002811.

Jamieson, R.A., Beaumont, C., Nguyen, M.H. & Grujic, D., 2006. Provenance of the Greater Himalayan Sequence and associated rocks; predictions of channel flow models. *Geological Society of London Special Publication,* **268,** 165–182.

Jessup, M. J., Cottle, M.J., Searle, M.P., Law, R.D., Newell, D.L., Tracy, R.J. & Waters, D.J., 2008. P–T–t–D paths of Everest Series schist, Nepal. *Journal of Metamorphic Geology,* **26,** 717–739.

Kohn, M.J., 2008. P-T-t data from Nepal support critical taper and repudiate large channel flow of the Greater Himalayan Sequence. *Geological Society of America Bulletin,* **120,** 259–273.

Kohn, M.J., 2014. Himalayan metamorphism and its tectonic implications. *Annual Review of Earth and Planetary Sciences,* **42,** 381–419.

Kohn, M.J., 2016, Metamorphic chronology comes of age: past achievements and future prospects. *American Mineralogist,* in press, doi:http://dx.doi.org/10.2138/am-2015-5146.

Kohn, M.J., Catlos, E., Ryerson, F.J. & Harrison, T.M., 2001. Pressure-Temperature-time path discontinuity in the Main Central thrust zone, Central Nepal. *Geology*, **29,** 571–574.

Larson, K.P., Godin, L. & Price, R.A., 2010. Relationships between displacement and distortion in orogens: linking the Himalayan foreland and hinterland in central Nepal. *Geological Society of American Bulletin,* **122,** 1116–1134.

926 Larson, K.P., Gervais, F. & Kellett, D.A, 2013. A P-T-t-D discontinuity in east-central Nepal:
927 Implications for the evolution of the Himalayan mid-crust. *Lithos*, **197,** 275–292.

928 Law, R.D., 2014. Deformation thermometry based on quartz c-axis fabric and recrystallization
929 microstructures: A review. *Journal of Structural Geology,* **66,** 129–161.

930 Law, R.D., Searle, M.P. & Simpson, R.L., 2004. Strain, deformation temperatures and vorticity of
931 flow at the top of the Greater Himalayan Slab, Everest Massif, Tibet. *Journal of the Geological*
932 *Society,* **161,** 305–320.

933 Le Fort, P., 1975. Himalaya, the collided range: Present knowledge of the continental arc. *American*
934 *Journal of Science,* **275A,** 1–44.

935 Le Fort, P. & France-Lanord, C., 1995. Granites form Mustang and surrounding regions (Central
936 Nepal). *Journal of Nepal Geological Society,* **11,** 53–57.

937 Massonne, H.-J., 2012. Formation of amphibole and clinozoisite-epidote in eclogite owing to fluid
938 infiltration during exhumation in a subduction channel. *Journal of Petrology,* **53,** 1969-1998.

939 Massonne, H.-J., 2014. Wealth of P–T–t information in medium-high grade metapelites: Example
940 from the Jubrique Unit of the Betic Cordillera, S Spain. *Lithos*, **208–209,** 137–157.

941 Montomoli, C., Iaccarino, S., Carosi, R., Langone, A. & Visonà, D., 2013. Tectonometamorphic
942 discontinuities within the Greater Himalayan Sequence in Western Nepal (Central Himalaya):
943 Insights on the exhumation of crystalline rocks. *Tectonophysics*, **608,** 1349–1370.

944 Montomoli, C., Carosi, R. & Iaccarino, S., 2015, Tectonometamorphic discontinuities in the Greater
945 Himalayan Sequence: a local or a regional feature? *Geological Society, London, Special*
946 *Publications,* **412,** 25–41.

947 Najman, Y., Bickle, M., BouDagher-Fadel, M., Carter A., Garzanti, E., Paul, M., Wijbrans, J.,
948 Willett E., Oliver, G., Parrish, R.R., Akhter S.H., Allen, R., Ando S., Chisty, E., Reisberg, L. &

949 Vezzoli, G., 2008. The Paleogene record of Himalayan erosion: Bengal Basin, Bangladesh. *Earth*
950 *and Planetary Science Letters*, **273,** 1–14.

951 Passchier, C.W. & Trouw, R.A. J., 2005. Microtectonics. II. Springer (Ed.), pp. 366.

952 Platt, J.P., 1993. Exhumation of high-pressure rocks: a review of concept and processes. *Terra*
953 *Nova,* **5,** 119–133.

954 Powell, R. & Holland, T., 1999. Relating formulations of the thermodynamics of mineral solid
955 solutions: activity modeling of pyroxenes, amphiboles, and micas. *American Mineralogist*, **84,** 1–
956 14.

957 Pyle, J. & Spear, F.S., 2000. An empirical garnet (YAG)-xenotime thermometer. *Contributions to*
958 *Mineralogy and Petrology,* **138,** 51-58.

959 Ramsay, J.G. & Huber, M.I., 1983. The Techniques of Modern Structural Geology: Strain
960 Analyses. London: Academic Press, pp. 307.

961 Ring, U., Brandon, M.T., Willett, S.D. & Lister, S. G., 1999. Exhumation processes. *Geological*
962 *Society, London, Special Publications,* **154,** 1–27.

963 Robinson, D.M., DeCelles, P.G. & Copeland, P., 2006. Tectonic evolution of the Himalayan thrust
964 belt in western Nepal: Implications for channel flow models. *Geological Society of America*
965 *Bulletin,* **118,** 865–885.

966 Rolfo, F., Groppo, C. & Mosca, P., 2015. Petrological constraints of the 'Channel Flow' model in
967 eastern Nepal. *Geological Society, London, Special Publications,* **412,** 177–197

968 Searle, M. P. & Godin, L., 2003. The South Tibetan Detachment System and the Manaslu
969 Leucogranite: a structural reinterpretation and restoration of the Annapurna–Manaslu Himalaya,
970 Nepal. *Journal of Geology,* **111,** 505–523.

971 Searle, M.P. & Szluc, A.G., 2005. Channel flow and ductile extrusion of the High Himalayan slab,
972 Kangchenjunga–Darjeeling profile, Sikkim Himalaya. *Journal of Asian Earth Sciences,* **25,** 173–
973 185.

974 Searle, M.P., Law, R.D., Godin, L., Larson, K., Streule, M.J., Cottle, J.M. & Jessup, M.J., 2008.
975 Defining the Himalayan Main Central Thrust in Nepal. *Journal of the Geological Society, London,*
976 **165,** 523–534.

977 Spear, F.S., 1993. Metamorphic Phase Equilibria and Pressure-Temperature-Time Paths, 799 p.
978 Mineralogical Society of America, Washington, D. C.

979 Spear, F.S., 2014. The duration of near-peak metamorphism from diffusion modelling of garnet
980 zoning. *Journal of Metamorphic Geology,* **32,** 903–914.

981 Spear, F.S. & Rumble, D., III, 1986. Pressure, temperature and structural evolution of the
982 Orfordville Belt, west-central New Hampshire. *Journal of Petrology,* **27,** 1071–1093.

983 Stephenson, B.J., Waters, D.J. & Searle, M.P., 2000. Inverted metamorphism and the main central
984 thrust: field relations and thermobarometric constraints from the Kishtwar Window, NW Indian
985 Himalaya. *Journal of Metamorphic Geology,* **18,** 571–590.

986 Stüwe, K., 1997. Effective bulk composition changes due to cooling: a model predicting
987 complexities in retrograde reaction textures. *Contributions to Mineralogy and Petrology,* **129,** 43–
988 52.

989 Stüwe, K. & Barr, T.D., 1998. On uplift and exhumation during convergence. *Tectonics*, **17,** 80–88.

990 Tajčmanová, L., Abart, R., Neusser, G. & Rhede, D., 2011. Growth of decompression plagioclase
991 rims around metastable kyanite from high-pressure felsic granulites (Bohemian Massif). *Journal of*
992 *Metamorphic Geology,* **29,** 1003–1018.

993 Teyssier, C., 2011. Exhumation of deep orogenic crust. *Lithosphere*, **3,** 439–443.

994 Tomkins, H.S., Powell, R. & Ellis, J., 2007. The pressure dependence of the zirconium-in-rutile
995 thermometer. *Journal of Metamorphic Geology,* **25,** 703–713.

996 Tracy, R.J., Robinson, P. & Thompson, A.B., 1976. Garnet composition and zoning in the
997 determination of temperature and pressure of metamorphism, central Massachusetts. *American*
998 *Mineralogist,* **61,** 762–775.

999 Vannay, J.C. & Hodges, K.V., 1996. Tectonometamorphic evolution of the Himalayan
1000 metamorphic core between the Annapurna and Dhaulaghiri, Central Nepal. *Journal of Metamorphic*
1001 *Geology,* **14,** 635–656.

1002 Vernon, R.H. 2011, Microstructures of melt-bearing regional metamorphic rocks. *Geological*
1003 *Society of America Memoirs*, **207,** 1–11.

1004 Visonà, D., Carosi, R., Montomoli, C., Peruzzo, L., & Tiepolo, M., 2012, Miocene andalusite
1005 leucogranite in central-east Himalaya (Everest–Masang Kang area): low-pressure melting during
1006 heating. *Lithos*, **144–145,** 194–208.

1007 Wang, J.M., Rubatto, D., & Zhang, J.J., 2015. Timing of partial melting and cooling across the
1008 Greater Himalayan Crystalline Complex (Nyalam, Central Himalaya): In-sequence thrusting and its
1009 implications: *Journal of Petrology,* **56**, 1677–1702.

1010 Weinberg, R. & Hasalová, P., 2015. Water-fluxed melting of the continental crust: A review.
1011 *Lithos*, **212–215,** 158–188.

1012 Weller, O.M., St-Onge, M.R., Waters, D.J., Rayner, N., Searle, M.P., Chung, S.-L., Palin, R.M.,
1013 Lee, Y. -H. & Xu, X., 2013. Quantifying Barrovian metamorphism in the Danba Structural
1014 Culmination of eastern Tibet. *Journal of Metamorphic Geology,* **31,** 909–935.

White, R.W., Powell, R. & Holland, T.J.B., 2001. Calculation of partial melting equilibria in the system Na_2O-CaO-K_2O-FeO-MgO-Al_2O_3-SiO_2-H_2O (NCKFMASH). *Journal of Metamorphic Geology,* **19,** 139–153.

White, R.W. & Powell, R., 2002. Melt loss and the preservation of granulite facies mineral assemblages. *Journal of Metamorphic Geology,* **20,** 621–632.

Willner, A.P., Sepúlveda, F. A., Hervé, F., Massonne, H.-J. & Sudo, M. 2009. Conditions and timing of pumpellyite-actinolite facies metamorphism in the Early Mesozoic frontal accretionary prism of the Madre de Dios Archipelago (50°20'S; southern Chile). *Journal of Petrology*, **50,** 2127–2155.

Yakymchuk, C. & Godin, L., 2012. Coupled role of deformation and metamorphism in the construction of inverted metamorphic sequences: an example from far northwest Nepal. *Journal of Metamorphic Geology,* **30,** 513–535.

Yakymchuk, C. & Brown, M., 2014. Consequences of open-system melting in tectonics. *Journal of the Geological Society, London,* **171,** 21–40.

LIST OF FIGURES

Figure 1. (a) Geological map of the Himalayan range (after Law *et al.,* 2004). The approximate location of Fig. 1b is reported; (b) Geological map of the Nepalese Himalaya (after Montomoli *et al.,* 2013 and references therein). The Mugu Karnali valley (study area) is shown; (c) Tectono-metamorphic map of the Mugu Karnali valley (Western Nepal). For simplicity only samples cited in the text or in Montomoli *et al.* (2013) are indicated. Cross section trace (A-A') of Fig. 2 is shown. In the inset, stereoplots of the main structural elements of LHS and GHS are reported (Wulff net – lower hemisphere). Abbreviations as follows: SSZ=Shyok suture zone; ZSZ=Zanskar shear zone; MKT=Main Karakoram Thrust; MMT=Main Mantle Thrust; TB=Tibetan Block; ITSZ=Indus

1039 Tsangpo Suture Zone; GCT=Great Counter Thrust; TSS=Tethyan Sedimentary Sequence;
1040 GHS=Greater Himalayan Sequence; STDS=South Tibetan Detachment System; MCT=Main
1041 Central Thrust; MBT=Main Boundary Thrust; MFT=Main Frontal Thrust; K=Kashmir basin;
1042 P=Peshawar basin; S=Sutlej basin.
1043
1044 Figure 2. Simplified geological cross-section (A-A', see Fig. 1c) along the Mugu Karnali transect.
1045 (a) L-tectonites (seen on two high angle surfaces) developed in chlorite-bearing quartzite (Grt I
1046 zone, LHS); (b) Garnet-staurolite porphyroblasts within a paragneiss (St + Bt ± Ky zone, GHS_L);
1047 (c) Large garnet porphyroblasts with internal foliation (S_i) in a garnet-kyanite-bearing paragneiss
1048 (St-out zone, GHS_L); (d) Mylonitic fabric reworking K-feldspar-, ± garnet-, ± aluminosilicates-
1049 bearing leucosomes, showing top-to the W/SW sense of shear in the Tiyar Shear Zone (TSZ) within
1050 the Kfs + Als zone (GHS_U); (e) Folded leucosomes in the garnet-bearing migmatite (Als + Kfs
1051 zone, GHS_U); (f) Flanking fold (N-type) pointing a top-to the E/SE sense of shear, within medium-
1052 low grade intercalations of phyllite and calsilicate (ES).
1053
1054 Figure 3. Meso- and microphotos of rocks from the migmatitic complex. (a) Garnet (arrow) bearing
1055 stromatic migmatite within the GHS_U; (b) Discordant leucocratic veinlet in an anatectic gneiss; (c)
1056 Euhedral mineral (arrow) included a plagioclase; (d) Feldspar film (arrow) around a corroded quartz
1057 grain; (e) Euhedral feldspar (arrow) within leucosome; (f) K-feldspar-bearing nanogranitoids
1058 (arrow) within peritectic garnet.
1059
1060 Figure 4. Representative garnet X-Ray compositional elementary (Mn, Ca, Mg, Fe) maps of
1061 selected samples from different structural position (see text for details). Colors were adjusted to best
1062 display the internal zoning.
1063

Figure 5. Chemical variation of main silicates in the studied samples. (a) garnet; (b) feldspar; (c) biotite; (d) potassic white mica. Abbreviations as follow: in Grt= inclusion in garnet; in St= inclusions in staurolite; Sp-1= older foliation preserved within microlithons; Sp = main foliation; post Sp = post-kinematic grain; +Sil = back reaction with biotite texturally associated with sillimanite.

Figure 6. (a) Crenulation cleavage and syn-tectonic garnet porphyroblast in D13-75 (LHS, Grt I zone); (b) Syn-tectonic plagioclase porphyroblast and biotite in LHS in D13-75 (LHS, Grt I zone); (c) General aspect of D13-06 (GHS_L, Grt II zone) showing skeletal garnet with asymmetric pressure shadows and late chlorite; (d) Garnet-staurolite-kyanite paragneiss of GHS_L (sample D09-10, St + Bt ± Ky zone). Note the garnet texture; (e) Syn-tectonic staurolite with S_i continuous with the external one (D09-10); (f) Garnet inclusion within staurolite porphyroblast (D09-10);

Figure 7. (a) Garnet-sillimanite bearing mylonitic paragneiss, sample D09-52 (GHS_U: Als + Wm zone); (b) Details of large kinked white mica (sample D09-52, GHS_U: Als + Wm zone); (c) K-feldspar porphyroclast with asymmetric myrmekite from sample D13-28 (GHS_U: Als + Kfs zone). Note the late white mica; d) Kyanite fish from D13-28 (GHS_U: Als + Kfs zone). Note the quartz-feldspar ribbons and the co-existence of sillimanite; (e) Boudinage of large pre-kinematic kyanite, with syn-kinematic sillimanite growth in the dilatational sites (sample D13-28); (f) Flattened garnet from sample D13-28. Note that the garnet edge is replaced by sillimanite+biotite.

Figure 8. (a) *P-T* pseudosection of D13-75 (LHS, Grt I zone). Observed mineral assemblage in bold; (b) *P-T* path from D13-75 sample, obtained with isopleths thermobarometry (ellipses); (c) *P-T* pseudosection for sample D13-06 (GHS_L, Grt II zone). In bold the observed mineral assemblage; (d) *P-T* path for D13-06 sample reconstructed with isopleths thermobarometry (ellipses).

Figure 9. (a) *P-T* pseudosection of D09-10 (GHS_L, St+Bt±Ky zone). In bold is reported the observed mineral assemblage in the sample; (b) Inferred *P-T* path for D09-10 sample, based on intersection of mineral compositions (ellipses). Grt in-R = garnet-in curve after garnet core fractionation (see also Fig. S4); (c) *P-T* pseudosection of sample D09-52 (GHS_U, Als+Wm zone); (d) Inferred *P-T* path of sample D09-52 based on compositional isopleths (ellipses) and minerals association (in bold in Fig. 9c).

Figure 10. (a) *P-T* pseudosection of D13-28 (GHS_U, Als + Kfs zone); (b) Proposed *P-T* path for D13-28 based on compositional isopleths (ellipses), minerals assemblages and Zr-in rutile thermometer.

Figure 11. Summary diagram showing pressure-temperature estimates and *P-T* paths along the Mugu Karnali. Symbols as in Fig. 1, see text for details.

LIST OF TABLES

Table 1. Representative EMP analyses (in wt.%) of garnet for the study samples. The garnet structural formula was recalculated on the basis of 24 O. Abbreviations as follows: c=core; r=rim; int=intermediate position (inner rim).

Table 2. Selected EMP analyses (in wt.%) of feldspars (Pl and Kfs). Structural formula was recalculated on the basis of 8 O. Abbreviations as follows: in-Grt=inclusion in garnet; m=matrix; n.a.=not analyzed. Mineral abbreviations as in the text.

Table 3. Representative EMP analyses (in wt.%) of biotite and chlorite in the study samples. Biotite structural formula was recalculated on the basis of 11 O, whereas 28 O was used for chlorite. Abbreviations as reported in Table 2.

Table 4. Selected EMP analyses (in wt.%) of white micas and staurolite in the study samples. Structural formula was recalculated on the basis of 11 O for white micas and on 46 O for staurolite. Abbreviations as in Table 2 plus f=large mica fish.

SUPPORTING INFORMATION

Supplementary figure captions

Fig. S1 – Sample D13-75 details of pseudosection calculation, with compositional isopleths: (a) XMn and XCa in garnet; (b) garnet XMg and Grt vol.% (100% solids) isomodes; (c) XMg in chlorite and Si a.p.f.u in white mica.

Fig. S2 – Sample D13-06 details of pseudosection calculation, with compositional isopleths: (a) XMn and XCa in garnet; (b) garnet XMg and Grt vol.% (100% solids) isomodes; (c) XMg in biotite and Si a.p.f.u in white mica.

Fig. S3 – Sample D09-10 details of pseudosection calculation, with compositional isopleths of: (a) garnet XMn and XCa; (b) garnet XMg and Grt vol.% (100% solids) isomodes; (c) XMg in biotite and Si a.p.f.u in white mica.

Fig. S4 – Sample D09-10 details of (a) *P-T* pseudosection after garnet core fractionation; and compositional isopleths of: (b) garnet XMn and XCa; (c) garnet XMg and Grt vol.% (100% solids) Grt isomodes; (d) XMg in biotite and Si a.p.f.u in white mica.

Fig. S5 – Sample D09-52 details of pseudosection calculation, with compositional isopleths of: (a) XMn and XCa in garnet; (b) garnet XMg and vol% (100% solids) Grt isomodes; (c) XMg in biotite and Si a.p.f.u in white mica.

Fig. S6 – T-XH_2O pseudosection for D13-28 at a fixed P of 0.70 GPa. On the abscissa axis H_2O wt% is reported. Arrow indicates the selected water amount for *P-T* pseudosection.

Fig. S7 – Sample D13-28 details of pseudosection calculation, with compositional isopleths of: (a) XCa and XFe in garnet; (b) XMg in biotite and XAb in plagioclase.

Fig. S8 – Examples of pristine rutile, coexisting with zircon, within sample D13-28.

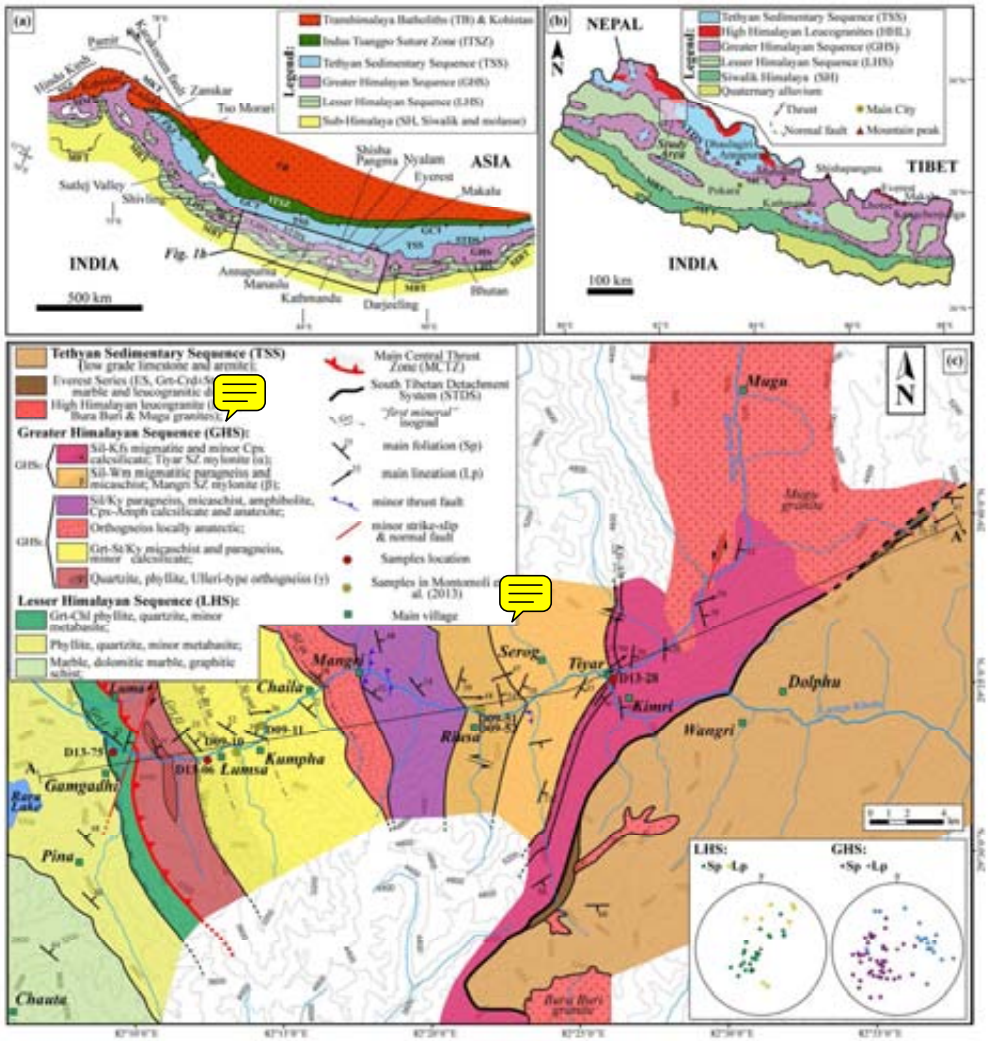

Figure 1. (a) Geological map of the Himalayan range (after Law et al., 2004). The approximate location of Fig. 1b is reported; (b) Geological map of the Nepalese Himalaya (after Montomoli et al., 2013 and references therein). The Mugu Karnali valley (study area) is shown; (c) Tectono-metamorphic map of the Mugu Karnali valley (Western Nepal). For simplicity only samples cited in the text or in Montomoli et al. (2013) are indicated. Cross section trace (A-A') of Fig. 2 is shown. In the inset, stereoplots of the main structural elements of LHS and GHS are reported (Wulff net – lower hemisphere). Abbreviations as follows: SSZ=Shyok suture zone; ZSZ=Zanskar shear zone; MKT=Main Karakoram Thrust; MMT=Main Mantle Thrust; TB=Tibetan Block; ITSZ=Indus Tsangpo Suture Zone; GCT=Great Counter Thrust; TSS=Tethyan Sedimentary Sequence; GHS=Greater Himalayan Sequence; STDS=South Tibetan Detachment System; MCT=Main Central Thrust; MBT=Main Boundary Thrust; MFT=Main Frontal Thrust; K=Kashmir basin; P=Peshawar basin; S=Sutlej basin.

150x156mm (300 x 300 DPI)

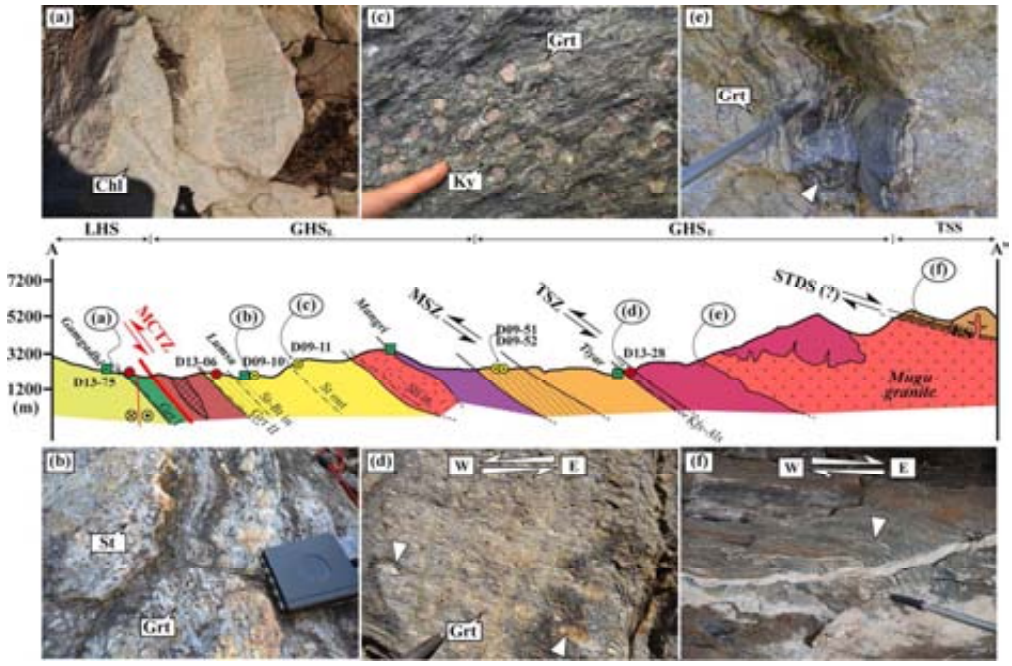

Figure 2. Simplified geological cross-section (A-A', see Fig. 1c) along the Mugu Karnali transect. (a) L-tectonites (seen on two high angle surfaces) developed in chlorite-bearing quartzite (Grt I zone, LHS); (b) Garnet-staurolite porphyroblasts within a paragneiss (St + Bt ± Ky zone, GHSL); (c) Large garnet porphyroblasts with internal foliation (Si) in a garnet-kyanite-bearing paragneiss (St-out zone, GHSL); (d) Mylonitic fabric reworking K-feldspar-, ± garnet-, ± aluminosilicates-bearing leucosomes, showing top-to the W/SW sense of shear in the Tiyar Shear Zone (TSZ) within the Kfs + Als zone (GHSU); (e) Folded leucosomes in the garnet-bearing migmatite (Als + Kfs zone, GHSU); (f) Flanking fold (N-type) pointing a top-to the E/SE sense of shear, within medium-low grade intercalations of phyllite and calsilicate (ES).

150x98mm (300 x 300 DPI)

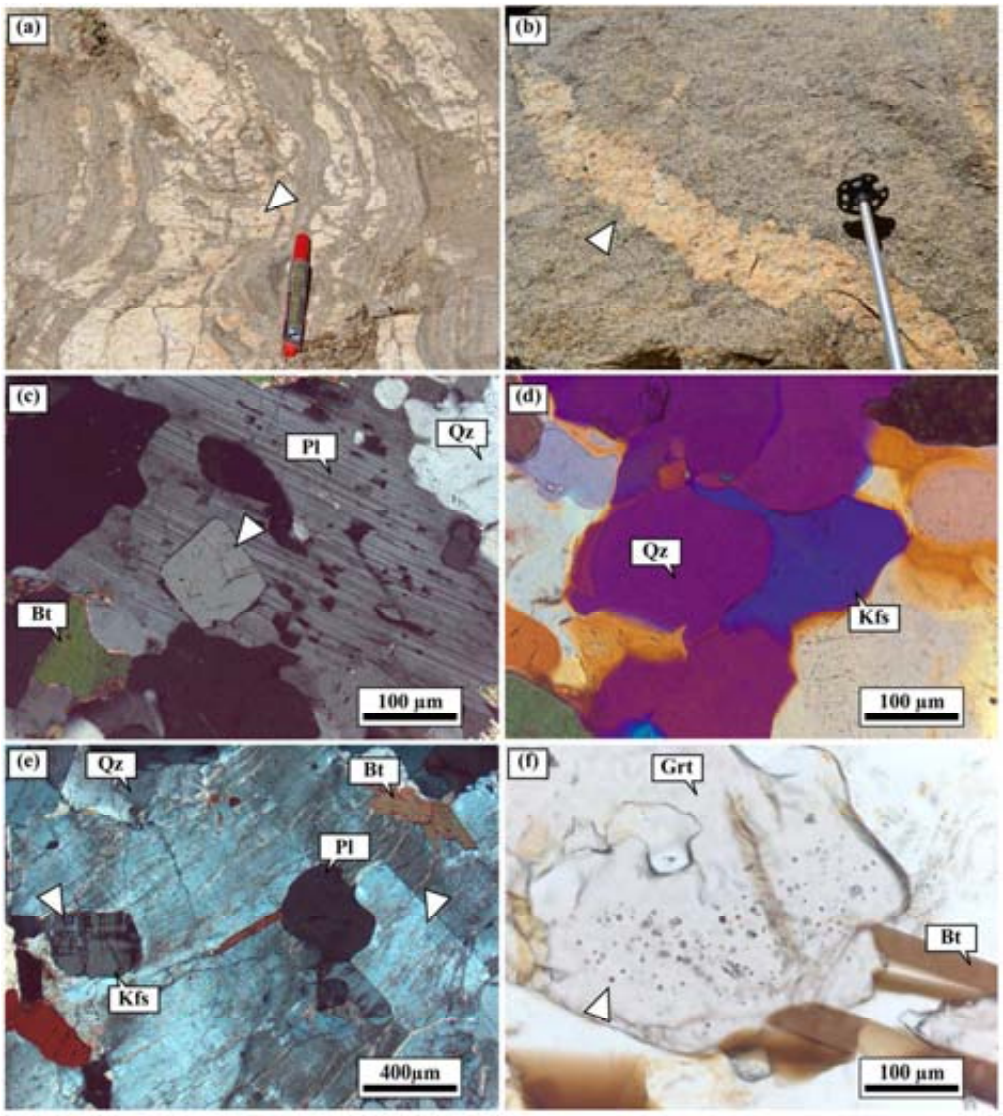

Figure 3. Meso- and microphotos of rocks from the migmatitic complex. (a) Garnet (arrow) bearing stromatic migmatite within the GHSU; (b) Discordant leucocratic veinlet in an anatectic gneiss; (c) Euhedral mineral (arrow) included a plagioclase; (d) Feldspar film (arrow) around a corroded quartz grain; (e) Euhedral feldspar (arrow) within leucosome; (f) K-feldspar-bearing nanogranitoids (arrow) within peritectic garnet.

150x166mm (300 x 300 DPI)

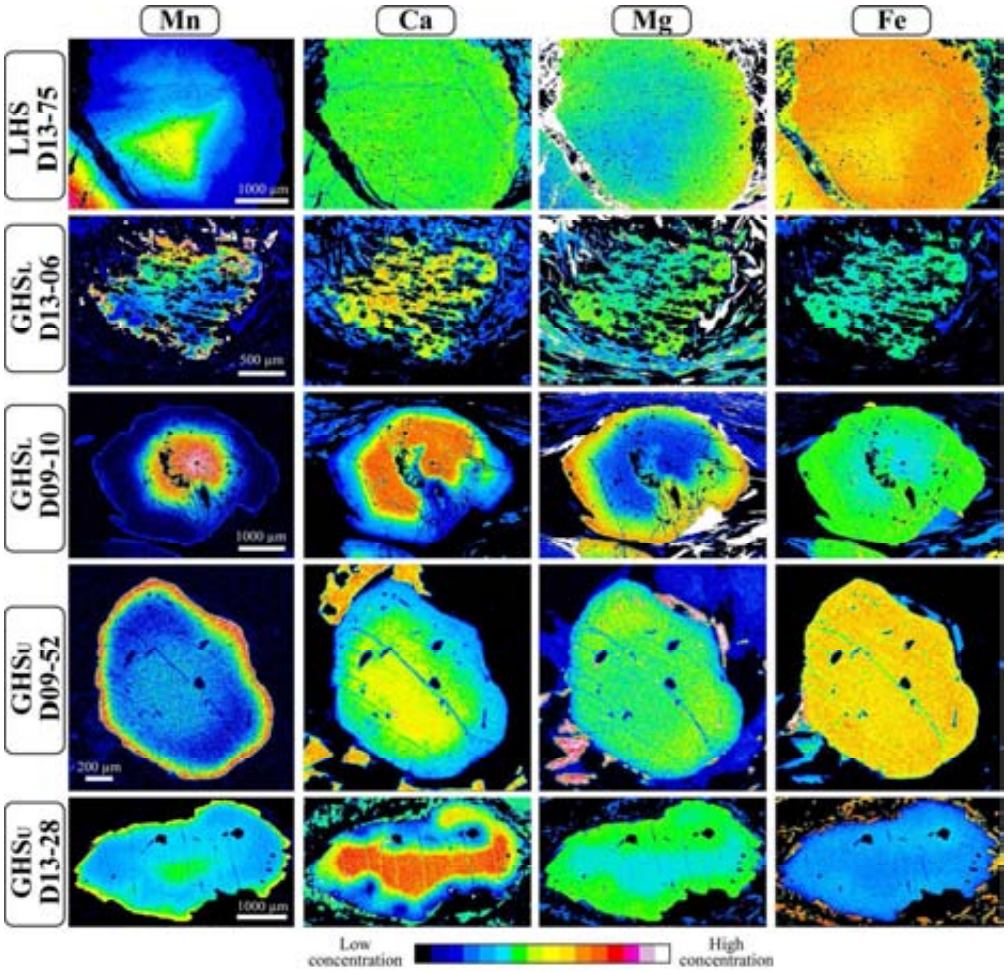

Figure 4. Representative garnet X-Ray compositional elementary (Mn, Ca, Mg, Fe) maps of selected samples from different structural position (see text for details). Colors were adjusted to best display the internal zoning

150x144mm (300 x 300 DPI)

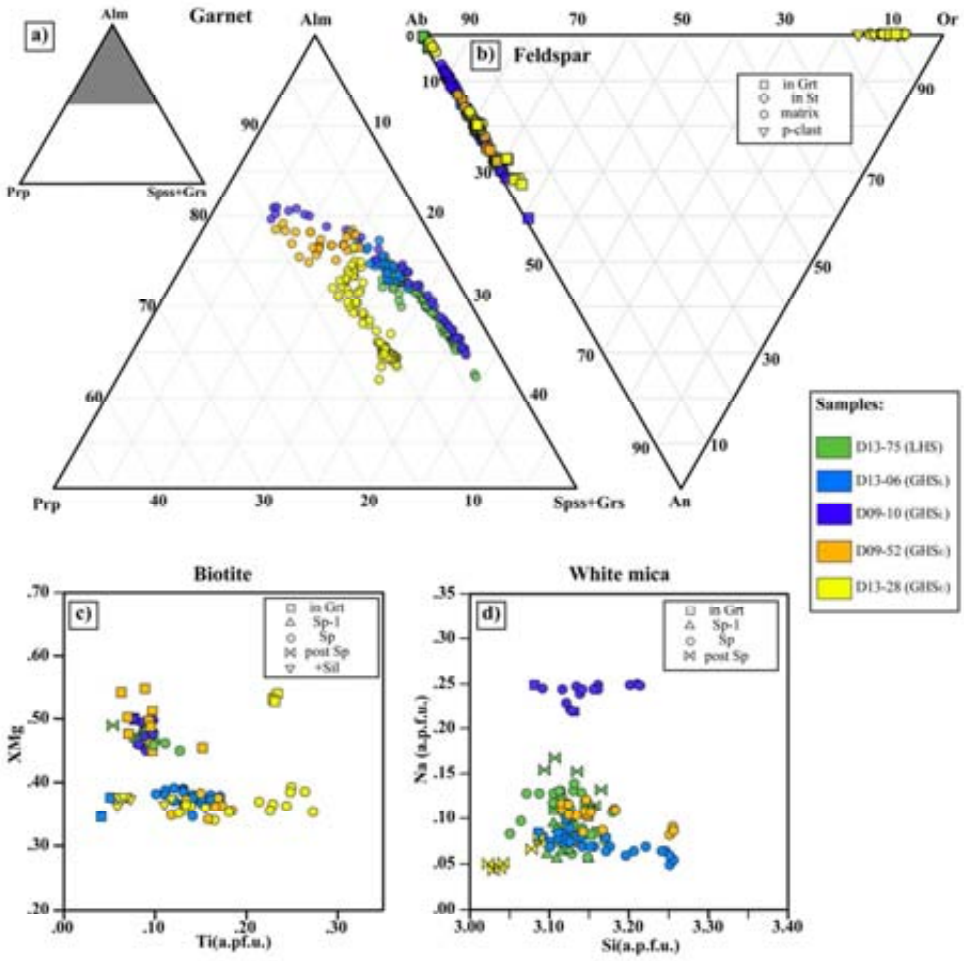

Figure 5. Chemical variation of main silicates in the studied samples. (a) garnet; (b) feldspar; (c) biotite; (d) potassic white mica. Abbreviations as follow: in Grt= inclusion in garnet; in St= inclusions in staurolite; Sp-1= older foliation preserved within microlithons; Sp = main foliation; post Sp = post-kinematic grain; +Sil = back reaction with biotite texturally associated with sillimanite.

153x156mm (300 x 300 DPI)

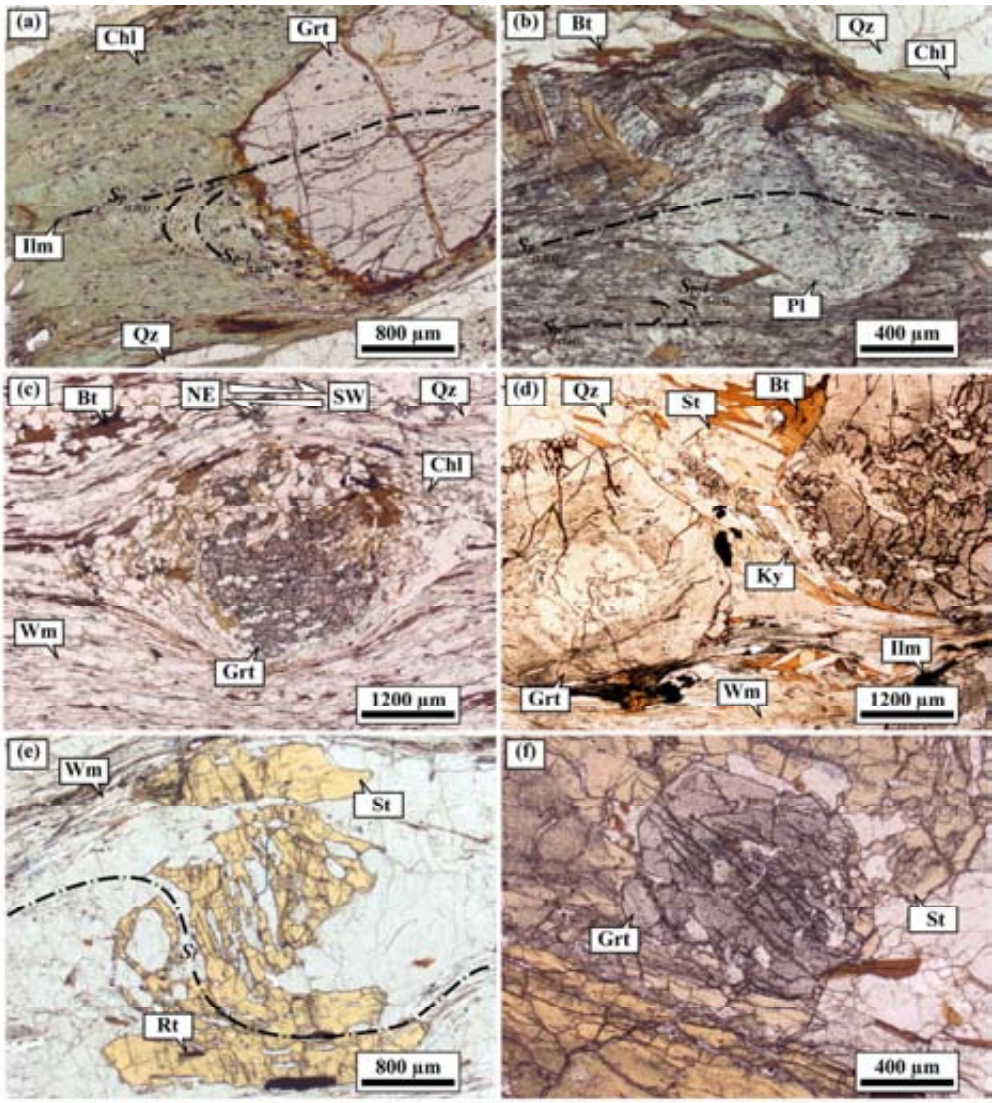

Figure 6. (a) Crenulation cleavage and syn-tectonic garnet porphyroblast in D13-75 (LHS, Grt I zone); (b) Syn-tectonic plagioclase porphyroblast and biotite in LHS in D13-75 (LHS, Grt I zone); (c) General aspect of D13-06 (GHSL, Grt II zone) showing skeletal garnet with asymmetric pressure shadows and late chlorite; (d) Garnet-staurolite-kyanite paragneiss of GHSL (sample D09-10, St + Bt ± Ky zone). Note the garnet texture; (e) Syn-tectonic staurolite with Si continuous with the external one (D09-10); (f) Garnet inclusion within staurolite porphyroblast (D09-10);

150x164mm (300 x 300 DPI)

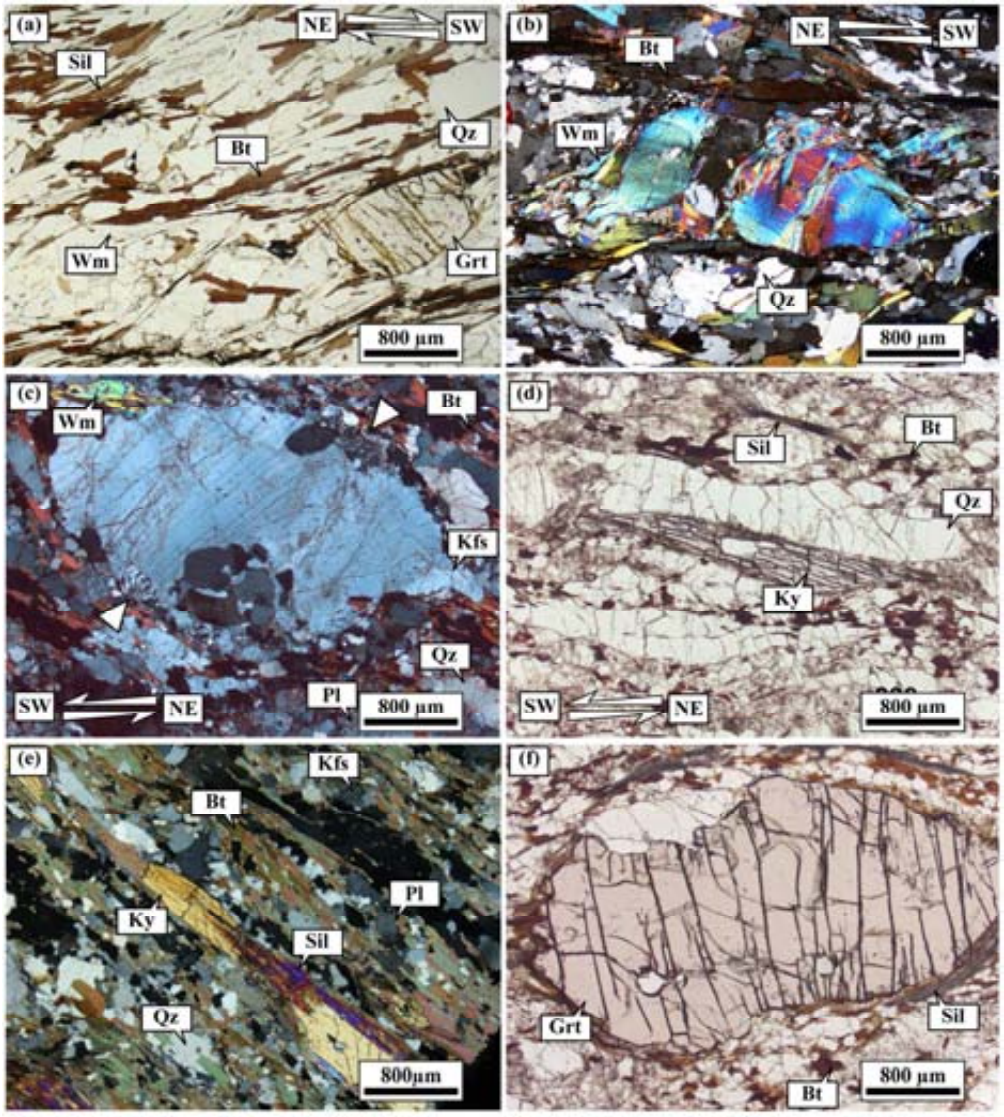

Figure 7. (a) Garnet-sillimanite bearing mylonitic paragneiss, sample D09-52 (GHSU: Als + Wm zone); (b) Details of large kinked white mica (sample D09-52, GHSU: Als + Wm zone); (c) K-feldspar porphyroclast with asymmetric myrmekite from sample D13-28 (GHSU: Als + Kfs zone). Note the late white mica; d) Kyanite fish from D13-28 (GHSU: Als + Kfs zone). Note the quartz-feldspar ribbons and the co-existence of sillimanite; (e) Boudinage of large pre-kinematic kyanite, with syn-kinematic sillimanite growth in the dilatational sites (sample D13-28); (f) Flattened garnet from sample D13-28. Note that the garnet edge is replaced by sillimanite+biotite.

150x167mm (300 x 300 DPI)

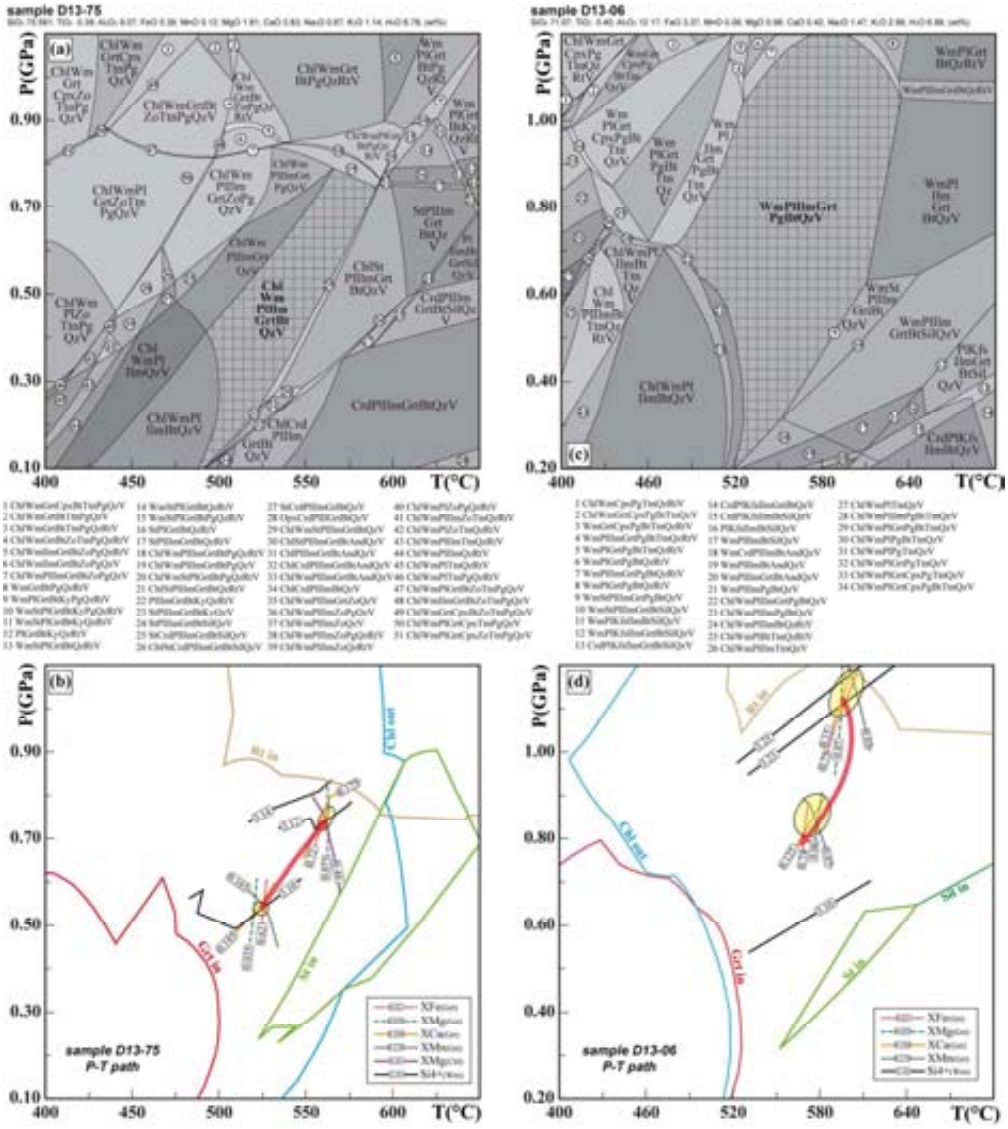

Figure 8. (a) P-T pseudosection of D13-75 (LHS, Grt I zone). Observed mineral assemblage in bold; (b) P-T path from D13-75 sample, obtained with isopleths thermobarometry (ellipses); (c) P-T pseudosection for sample D13-06 (GHSL, Grt II zone). In bold the observed mineral assemblage; (d) P-T path for D13-06 sample reconstructed with isopleths thermobarometry (ellipses).

150x168mm (300 x 300 DPI)

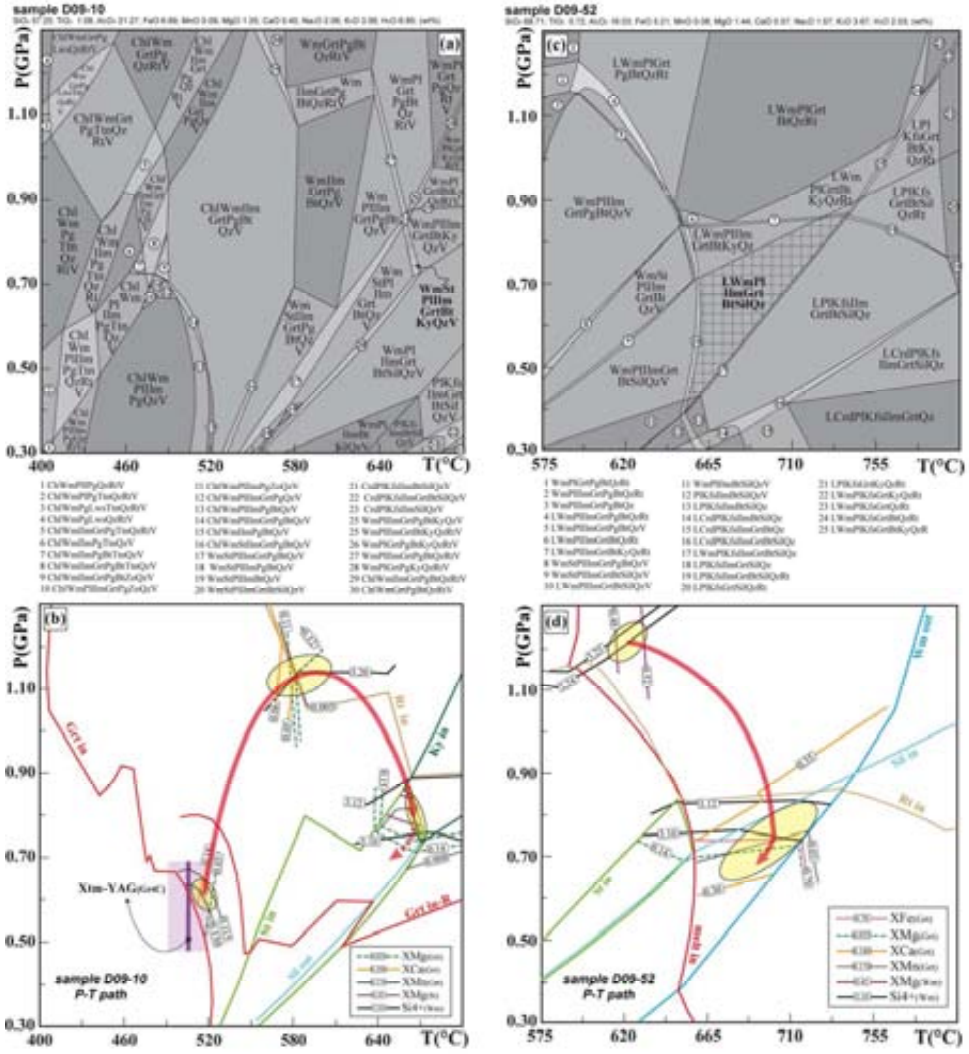

Figure 9. (a) P-T pseudosection of D09-10 (GHSL, St+Bt±Ky zone). In bold is reported the observed mineral assemblage in the sample; (b) Inferred P-T path for D09-10 sample, based on intersection of mineral compositions (ellipses). Grt in-R = garnet-in curve after garnet core fractionation (see also Fig. S4); (c) P-T pseudosection of sample D09-52 (GHSU, Als+Wm zone); (d) Inferred P-T path of sample D09-52 based on compositional isopleths (ellipses) and minerals association (in bold in Fig. 9c).

150x162mm (300 x 300 DPI)

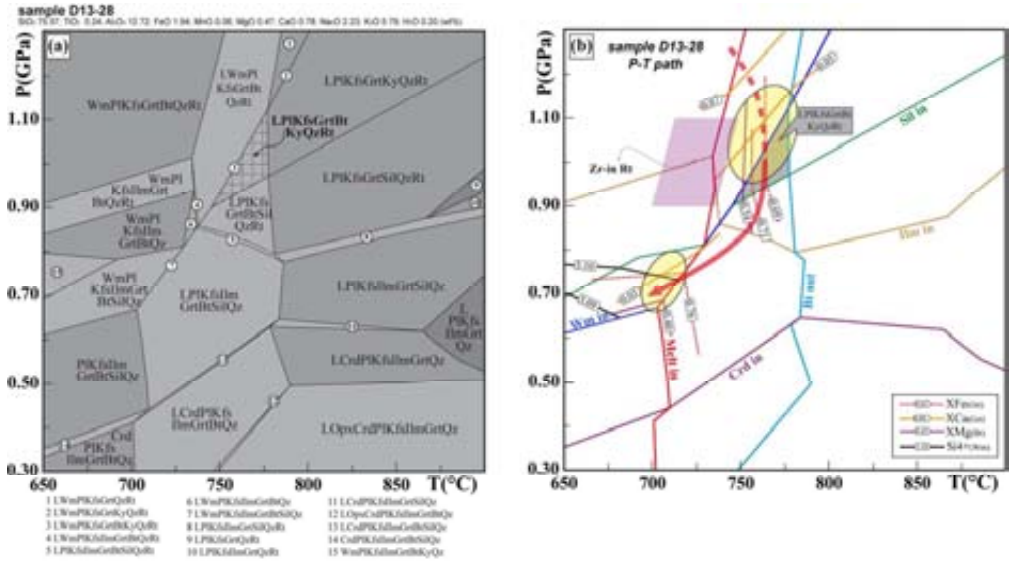

Figure 10. (a) P-T pseudosection of D13-28 (GHSU, Als + Kfs zone); (b) Proposed P-T path for D13-28 based on compositional isopleths (ellipses), minerals assemblages and Zr-in rutile thermometer.

150x85mm (300 x 300 DPI)

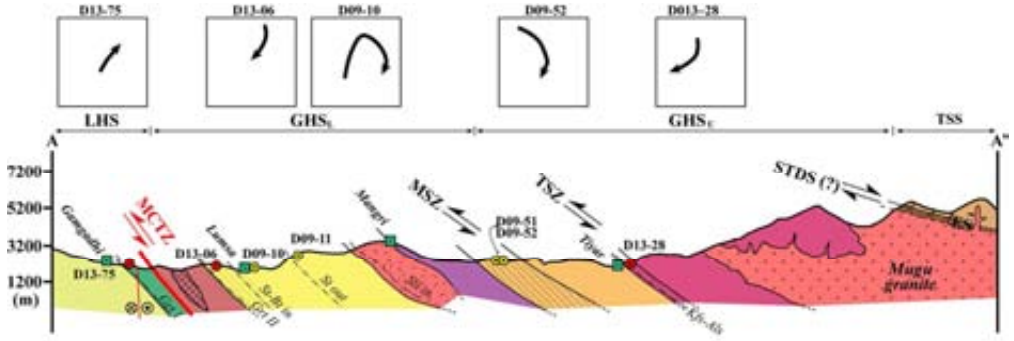

Figure 11. Summary diagram showing pressure-temperature estimates and P-T paths along the Mugu Karnali. Symbols as in Fig. 1, see text for details.

150x51mm (300 x 300 DPI)

Table 1

sample	D13-75	D13-75	D13-75	D13-06	D13-06	D13-06	D09-10	D09-10	D09-10	D09-52	D09-52	D09-52	D13-28	D13-28	D13-28
position	c	int	r	c	int	r	c	int	r	c	int	r	c	int	r
SiO_2	35.26	36.80	36.98	36.55	36.41	36.08	37.61	37.40	36.91	38.07	38.24	37.15	34.87	34.79	34.58
TiO_2	0.13	0.07	0.02	0.05	0.04	0.04	0.10	0.01	0.01	0.00	0.07	0.03	0.00	0.02	0.01
Al_2O_3	20.69	21.32	21.81	21.36	21.04	21.15	22.07	22.30	22.45	20.69	21.01	21.36	20.58	20.86	20.87
Cr_2O_3	0.04	0.02	0.01	0.01	0.02	0.02	0.00	0.02	0.06	0.05	0.04	0.00	0.00	0.02	0.01
FeO_{tot}	29.48	33.93	33.37	33.47	33.74	33.11	30.00	37.11	37.16	33.29	36.19	35.20	32.27	34.52	35.61
MnO	6.89	2.18	1.08	1.36	2.16	2.88	5.63	0.16	0.61	3.07	0.79	4.97	2.00	1.95	3.52
MgO	0.86	1.22	1.93	1.70	1.56	1.58	0.83	3.08	3.38	2.42	3.73	1.88	2.84	2.80	1.98
CaO	6.42	6.19	6.36	5.18	4.90	4.38	6.51	2.33	1.58	3.57	1.82	1.09	5.47	3.99	2.53
Na_2O	0.02	0.02	0.01	0.03	0.02	0.03	0.00	0.01	0.00	0.00	0.01	0.00	0.02	0.02	0.02
Total	99.90	101.75	101.56	99.71	99.91	99.25	102.75	102.41	102.17	101.22	101.96	101.68	98.32	98.98	99.13
Si	5.59	5.76	5.76	5.85	5.83	5.80	5.87	5.79	5.69	6.11	6.02	5.92	5.52	5.46	5.54
Ti	0.02	0.01	0.00	0.01	0.01	0.00	0.01	0.00	0.00	0.00	0.00	0.00	0.00	0.00	0.00
Al	3.86	3.93	4.00	4.03	3.97	4.01	4.06	4.07	4.08	3.91	3.90	4.01	3.84	3.86	3.87
Cr	0.01	0.00	0.00	0.00	0.03	0.00	0.00	0.02	0.01	0.01	0.00	0.00	0.00	0.00	0.00
Fe^{3+}	0.13	0.06	0.00	0.00	0.03	0.00	0.00	0.00	0.00	0.08	0.02	0.00	0.16	0.14	0.13
Fe^{2+}	3.78	4.38	4.34	4.48	4.49	4.45	3.92	4.81	4.79	4.39	4.74	4.69	4.13	4.41	4.62
Mn	0.93	0.29	0.14	0.18	0.29	0.39	0.74	0.02	0.08	0.42	0.10	0.67	0.27	0.26	0.47
Mg	0.20	0.29	0.45	0.40	0.37	0.38	0.19	0.71	0.78	0.58	0.88	0.45	0.67	0.66	0.47
Ca	1.09	1.04	1.06	0.89	0.84	0.75	1.09	0.39	0.26	0.61	0.30	0.19	0.93	0.67	0.43
Na	0.01	0.01	0.00	0.01	0.01	0.01	0.00	0.00	0.00	0.00	0.00	0.00	0.01	0.01	0.01

Table 2

sample	D13-75	D13-75	D13-75	D13-06	D13-06	D13-06	D09-10	D09-10	D09-52	D09-52	D09-52	D13-28	D13-28	D13-28	D13-28	D13-28
mineral	Pl	Pl	Pl	Pl	Pl	Pl	Pl	Pl	Pl	Pl	Pl	Pl	Pl	Pl	Kfs	Kfs
position	in-Grt	m-c	m-r	in-Grt	m-c	m-r	m-c	m-r	in-Grt	m-c	m-r	in-Grt	m-c	m-r	in-Grt	m
SiO_2	62.98	62.14	61.38	62.22	64.54	64.36	65.76	64.80	62.00	65.98	64.95	57.54	61.55	61.60	63.07	62.93
Al_2O_3	22.56	24.52	24.56	23.40	21.34	21.52	21.89	21.85	24.14	21.56	22.43	23.77	21.80	22.52	17.98	18.03
FeO_{tot}	1.02	0.26	0.45	0.22	0.08	0.11	0.18	0.12	0.17	0.03	0.11	0.15	0.09	0.08	0.03	0.02
MgO	0.03	0.00	0.01	0.00	0.01	0.00	0.00	0.00	0.00	0.00	0.00	0.04	0.00	0.00	0.00	0.01
BaO	0.00	0.00	0.00	0.02	0.00	0.00	n.a.	n.a.	n.a.	n.a.	n.a.	0.00	0.00	0.00	0.17	0.11
CaO	4.18	6.11	6.05	4.70	2.66	2.79	1.87	1.64	5.76	2.70	3.73	6.97	3.62	4.11	0.02	0.08
Na_2O	8.97	7.97	8.20	9.25	10.33	10.24	10.09	10.67	8.10	9.74	9.09	7.55	9.81	9.51	1.04	1.16
K_2O	0.09	0.10	0.09	0.07	0.09	0.07	0.11	0.12	0.13	0.09	0.12	0.50	0.20	0.11	15.63	15.68
Total	99.83	101.10	100.74	99.87	99.04	99.08	99.90	99.20	100.30	100.10	100.43	96.52	97.07	97.93	97.94	98.02
Si	2.80	2.73	2.71	2.76	2.87	2.86	2.91	2.89	2.74	2.88	2.85	2.67	2.81	2.79	2.99	2.98
Al	1.18	1.27	1.28	1.22	1.12	1.13	1.11	1.13	1.26	1.14	1.16	1.30	1.17	1.20	1.00	1.01
Fe^{2+}	0.03	0.01	0.02	0.01	0.00	0.00	0.00	0.01	0.01	0.00	0.01	0.01	0.00	0.00	0.00	0.00
Mg	0.00	0.00	0.00	0.00	0.00	0.00	0.00	0.00	0.00	0.00	0.00	0.00	0.00	0.00	0.00	0.00
Ba	0.00	0.00	0.00	0.00	0.00	0.00	–	–	–	–	–	0.00	0.00	0.00	0.00	0.00
Ca	0.20	0.29	0.29	0.22	0.13	0.13	0.11	0.09	0.27	0.14	0.18	0.35	0.18	0.20	0.00	0.00
Na	0.77	0.68	0.70	0.80	0.89	0.88	0.81	0.86	0.70	0.81	0.77	0.68	0.87	0.84	0.10	0.11
K	0.01	0.01	0.01	0.00	0.01	0.00	0.01	0.01	0.01	0.01	0.01	0.03	0.01	0.01	0.94	0.95

Table 3

sample	D13-75	D13-75	D13-75	D13-75	D13-06	D13-06	D09-10	D09-10	D09-52	D09-52	D13-28	D13-28	D13-28
mineral	Bt	Bt	Chl	Chl	Bt	Bt	Bt	Bt	Bt	Bt	Bt	Bt	Bt
position	in-Grt	m	in-Grt	m	in-Grt	m	in-Grt	m	in-Grt	m	in-Grt	m	m
SiO_2	36.21	36.19	25.13	24.80	33.93	35.09	36.24	37.92	36.99	36.10	35.20	33.96	33.68
TiO_2	1.54	1.52	0.10	0.09	0.76	2.38	0.83	1.38	1.64	2.65	4.08	4.65	1.15
Al_2O_3	16.85	17.73	21.99	22.73	18.10	17.24	19.29	19.29	20.10	20.15	18.88	17.42	19.55
FeO_{tot}	21.17	19.67	28.02	27.98	23.45	23.06	0.01	19.03	18.25	21.79	15.58	22.34	22.27
MnO	0.11	0.10	0.52	0.15	0.14	0.10	21.92	0.00	0.06	0.13	0.02	0.19	0.09
MgO	10.30	10.15	13.03	13.29	7.93	7.63	8.93	10.66	10.17	7.63	10.32	6.91	7.57
BaO	0.10	0.09	0.00	0.00	0.05	0.17	n.a.	n.a.	n.a.	n.a.	0.12	0.13	0.03
CaO	0.11	0.02	0.10	0.02	0.03	0.00	0.03	0.00	0.13	0.04	0.05	0.00	0.03
Na_2O	0.13	0.13	0.03	0.00	0.12	0.09	0.21	0.30	0.28	0.26	0.26	0.09	0.09
K_2O	9.17	9.63	0.02	0.05	9.71	9.45	7.95	7.88	8.68	8.66	9.89	10.02	9.87
Total	95.69	95.23	88.94	89.11	94.22	95.21	95.40	96.46	96.31	97.40	94.40	95.71	94.33
Si	2.77	2.77	5.30	5.21	2.69	2.73	2.75	2.79	2.74	2.69	2.67	2.64	2.65
Ti	0.09	0.09	0.02	0.02	0.05	0.19	0.05	0.08	0.09	0.15	0.23	0.27	0.07
Al	1.52	1.60	5.47	5.63	1.69	1.58	1.73	1.70	1.76	1.77	1.69	1.60	1.81
Fe^{2+}	1.35	1.26	4.94	4.92	1.55	1.50	1.39	1.16	1.13	1.13	0.99	1.45	1.46
Mn	0.01	0.01	0.09	0.03	0.01	0.01	0.00	0.00	0.00	0.00	0.00	0.01	0.01
Mg	1.18	1.16	4.10	4.16	0.94	0.89	1.01	1.14	1.12	1.12	1.17	0.80	0.89
Ba	0.00	0.00	0.00	0.00	0.00	0.01	–	–	–	–	0.00	0.00	0.00
Ca	0.01	0.00	0.02	0.00	0.00	0.00	0.00	0.00	0.01	0.01	0.00	0.00	0.00
Na	0.02	0.02	0.01	0.00	0.02	0.01	0.03	0.05	0.04	0.04	0.04	0.01	0.01
K	0.90	0.94	0.01	0.01	0.98	0.95	0.77	0.76	0.82	0.82	0.96	1.00	0.99

Table 4

sample	D13-75	D13-75	D13-06	D13-06	D09-10	D09-10	D09-10	D09-10	D09-52	D09-52	D13-28	D13-28	D09-10	D09-10
mineral	Wm	Wm	Wm	Wm	Pg	Wm	Wm	Wm	Wm	Wm	Wm	Wm	St	St
position	in-Grt	m	m	m	in-Grt	in-Grt	m	m	f	m	m	m	c	r
SiO_2	46.68	47.13	47.78	46.26	31.93	47.13	49.10	48.30	48.70	48.17	46.17	44.74	28.56	28.58
TiO_2	0.24	0.26	0.63	0.68	0.21	0.48	0.65	0.53	0.93	0.85	0.53	0.00	0.79	0.68
Al_2O_3	34.55	34.33	30.27	33.86	48.39	36.89	34.72	36.51	31.94	36.21	34.44	36.05	52.32	51.39
FeO_{tot}	1.79	1.51	2.28	2.05	1.39	0.95	1.20	1.02	1.79	1.24	2.28	0.77	13.84	13.60
ZnO	n.a.	n.a.	n.a.	n.a.	n.a.	n.a.	n.a.	n.a.	n.a.	n.a.	n.a.	n.a.	0.32	0.27
MnO	0.04	0.04	0.00	0.00	0.03	0.01	0.00	0.00	0.02	0.05	0.07	0.00	0.07	0.05
MgO	1.09	1.16	1.85	1.10	0.17	0.45	0.49	0.51	1.15	0.49	0.67	0.26	1.60	1.55
BaO	0.13	0.07	0.18	0.21	n.a.	n.a.	n.a.	n.a.	n.a.	n.a.	b.d.	b.d.	n.a.	n.a.
CaO	0.03	0.01	0.01	0.02	10.86	0.03	0.08	0.00	0.04	0.01	0.07	0.02	0.00	0.01
Na_2O	0.86	1.12	0.51	0.58	1.55	1.99	1.99	1.84	0.64	0.94	0.59	0.39	n.a.	n.a.
K_2O	10.23	9.63	10.65	10.51	0.02	7.07	7.09	7.49	8.77	9.03	10.91	11.21	0.01	0.00
Total	95.64	95.26	94.16	95.26	94.55	95.00	95.33	96.20	93.98	97.00	95.73	97.86	97.52	96.14
Si	3.10	3.13	3.24	3.10	2.14	3.08	3.20	3.12	3.25	3.11	3.09	3.04	7.95	8.07
Ti	0.01	0.01	0.03	0.03	0.01	0.02	0.03	0.03	0.05	0.042	0.03	0.00	0.17	0.15
Al	2.71	2.69	2.42	2.67	3.82	2.84	2.67	2.78	2.51	2.76	2.71	2.89	17.18	17.09
Fe^{2+}	0.10	0.08	0.13	0.11	0.08	0.05	0.07	0.06	0.10	0.07	0.13	0.04	3.23	3.20
Zn	–	–	–	–	–	–	–	–	–	–	–	–	0.07	0.05
Mn	0.00	0.00	0.00	0.00	0.00	0.00	0.00	0.00	0.00	0.00	0.01	0.00	0.02	0.02
Mg	0.11	0.12	0.19	0.11	0.02	0.04	0.05	0.05	0.11	0.05	0.07	0.03	0.67	0.64
Ba	0.00	0.00	0.00	0.01	–	–	–	–	–	–	0.08	0.00	–	–
Ca	0.00	0.00	0.00	0.00	0.78	0.00	0.01	0.00	0.00	0.00	0.00	0.00	0.00	0.00
Na	0.11	0.14	0.07	0.07	0.20	0.25	0.25	0.23	0.08	0.12	0.08	0.05	–	–
K	0.87	0.82	0.92	0.90	0.00	0.59	0.59	0.62	0.75	0.75	0.93	0.97	0.00	0.00

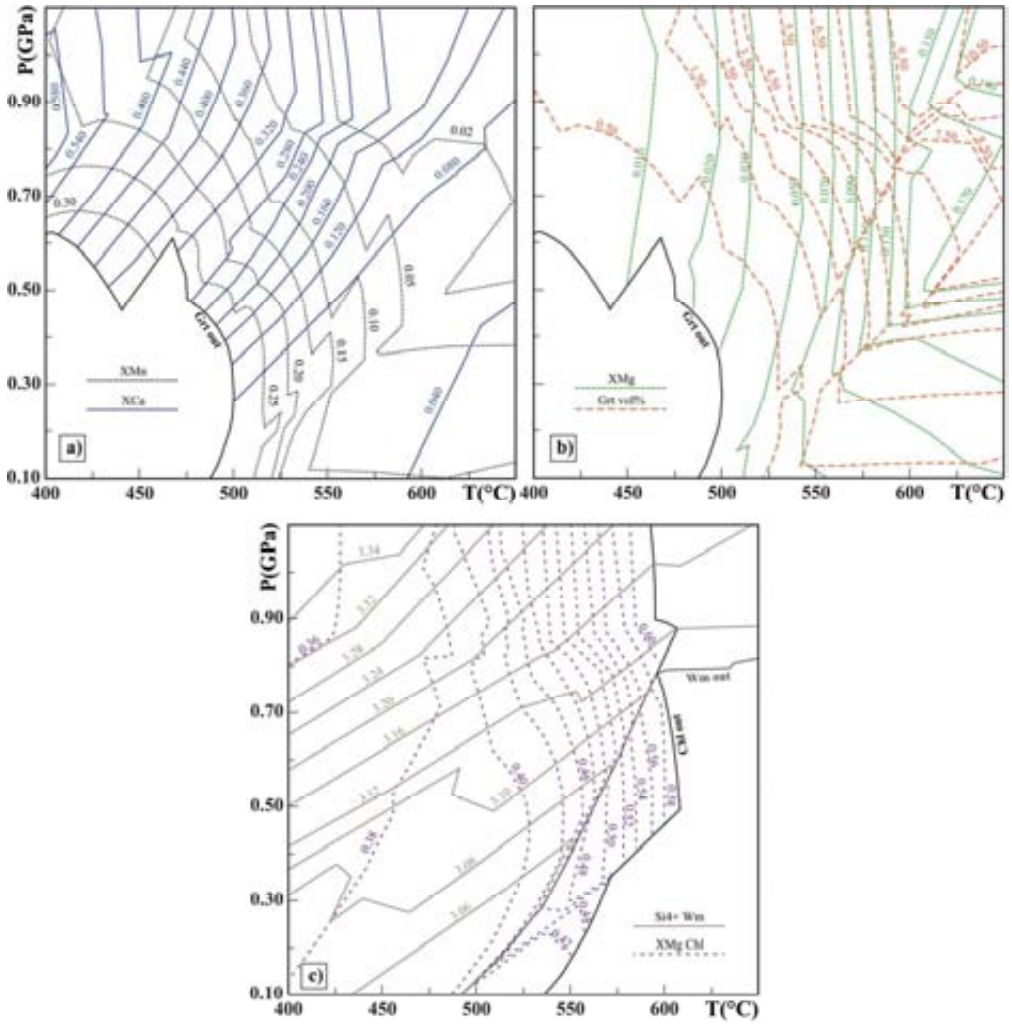

Fig. S1

150x162mm (300 x 300 DPI)

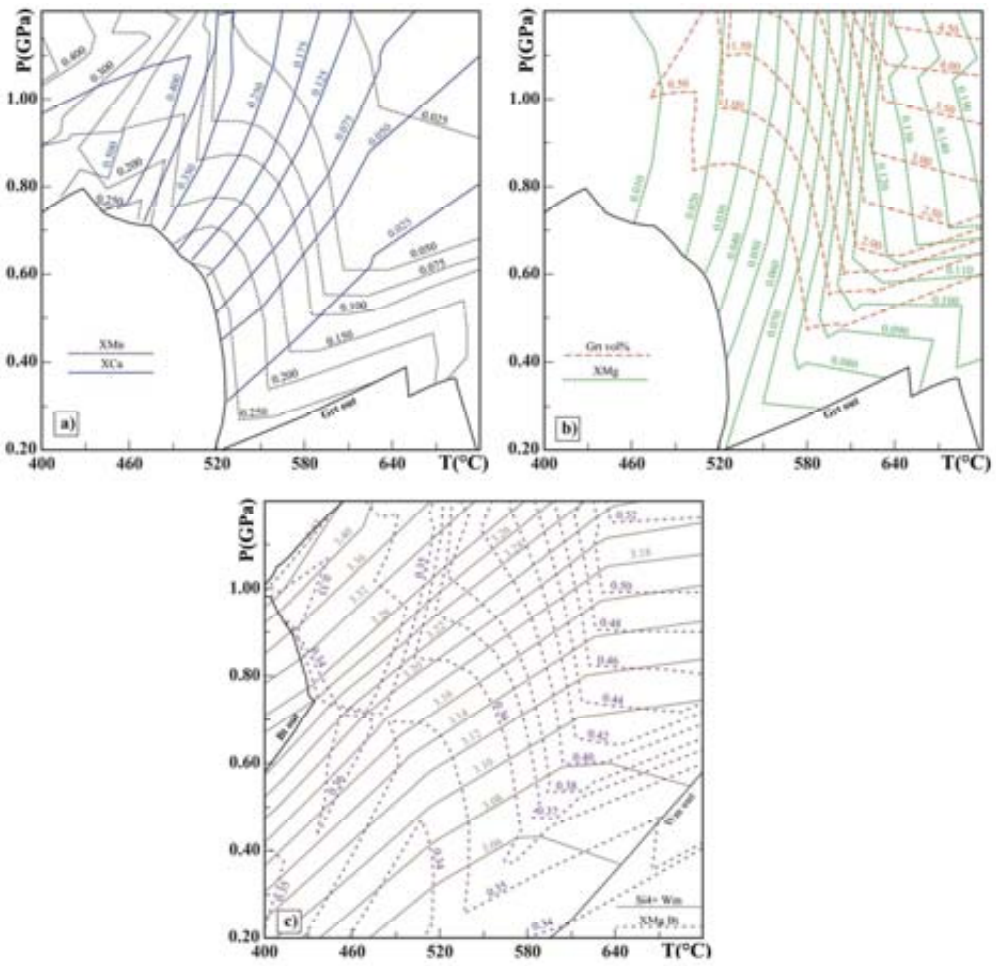

Fig. S2

150x152mm (300 x 300 DPI)

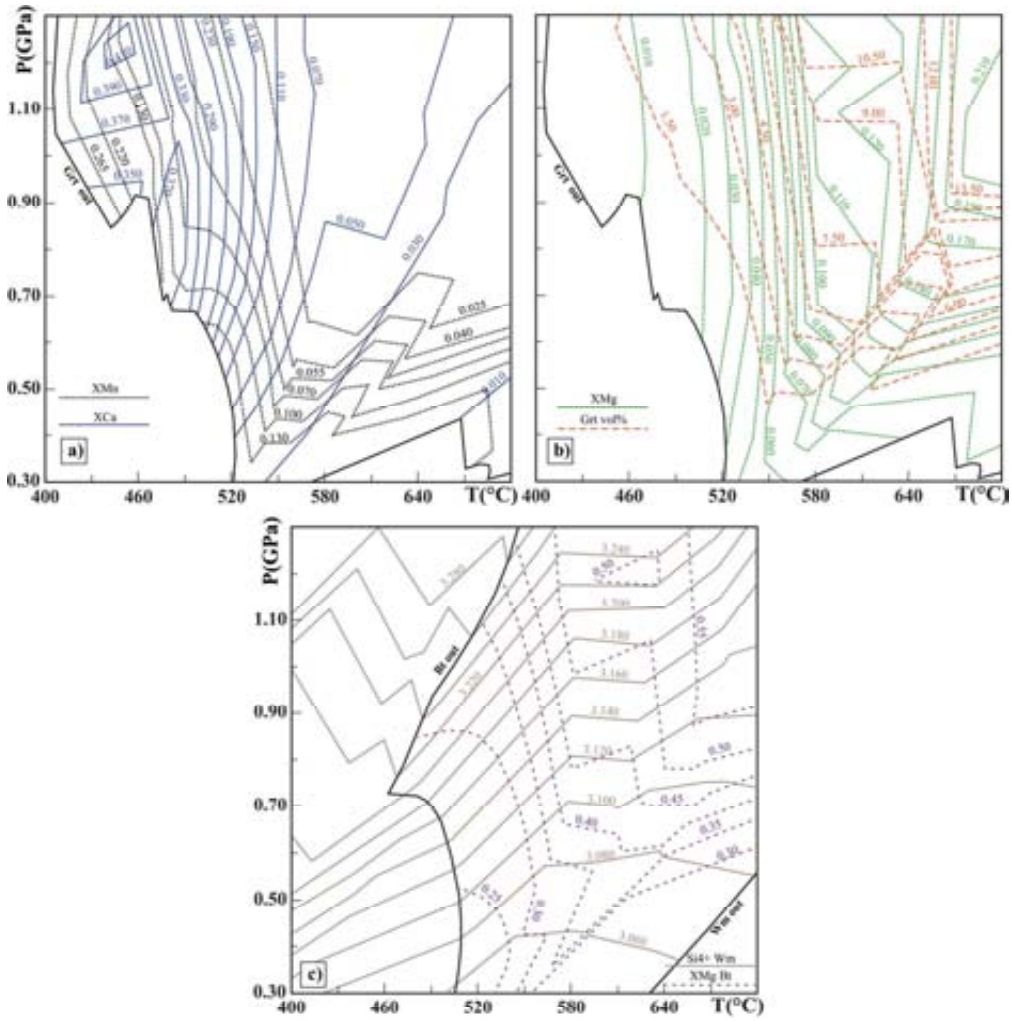

Fig. S3

150x165mm (300 x 300 DPI)

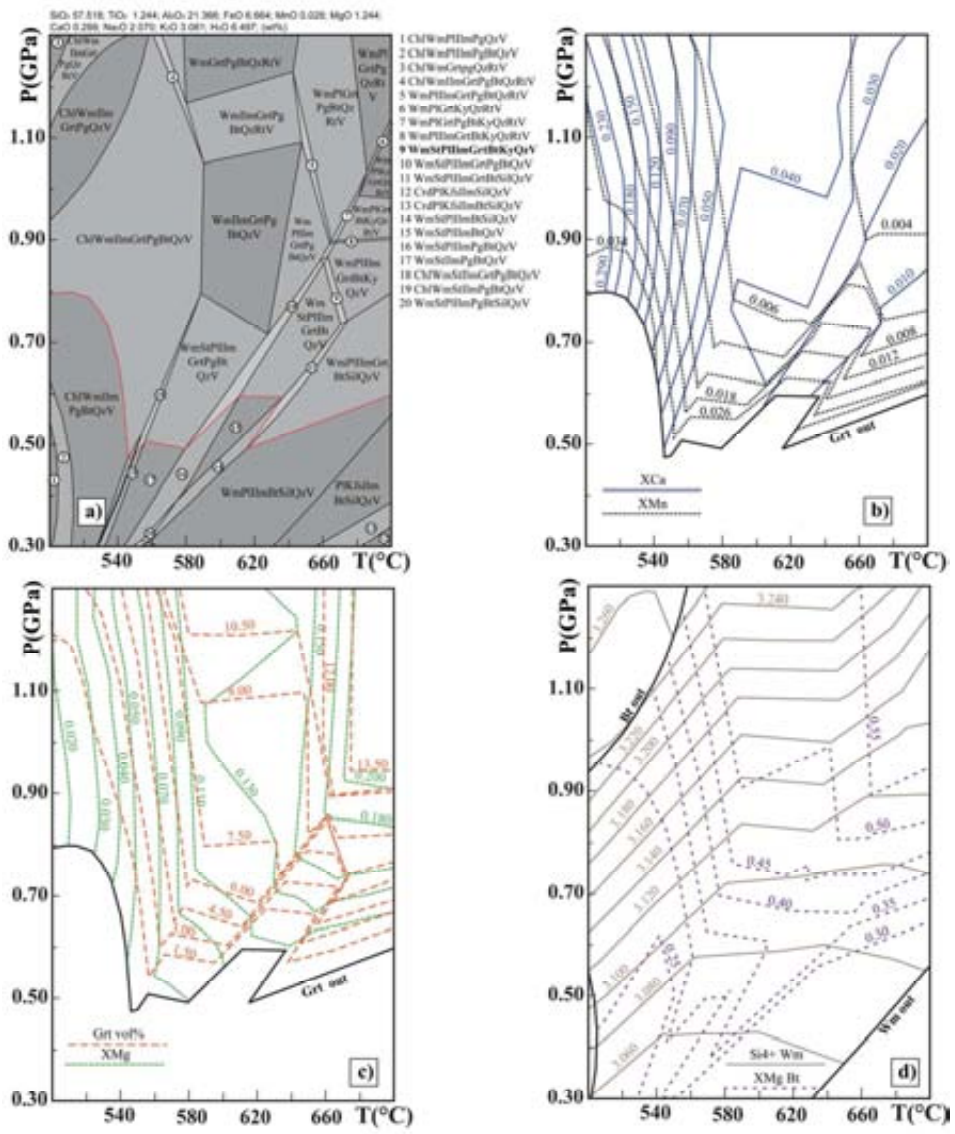

Fig. S4

150x189mm (300 x 300 DPI)

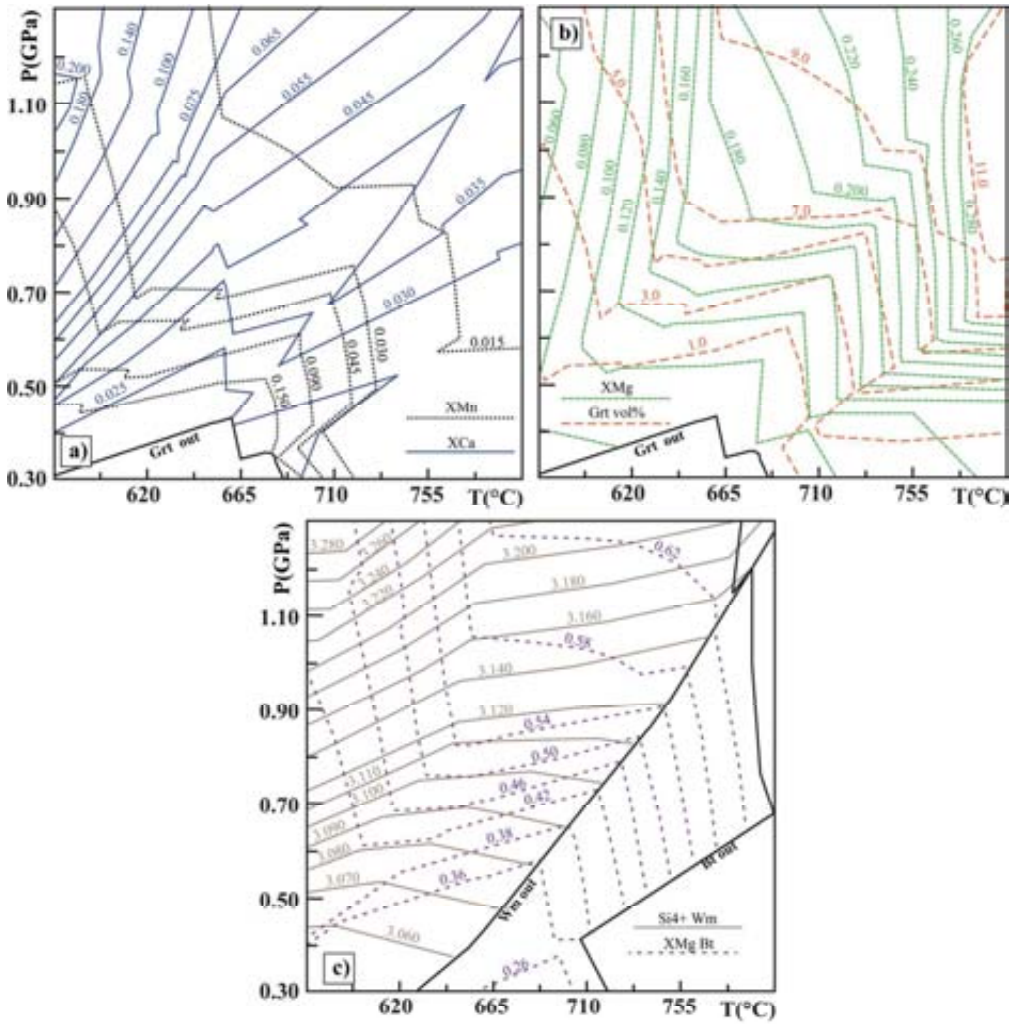

Fig. S5

150x165mm (300 x 300 DPI)

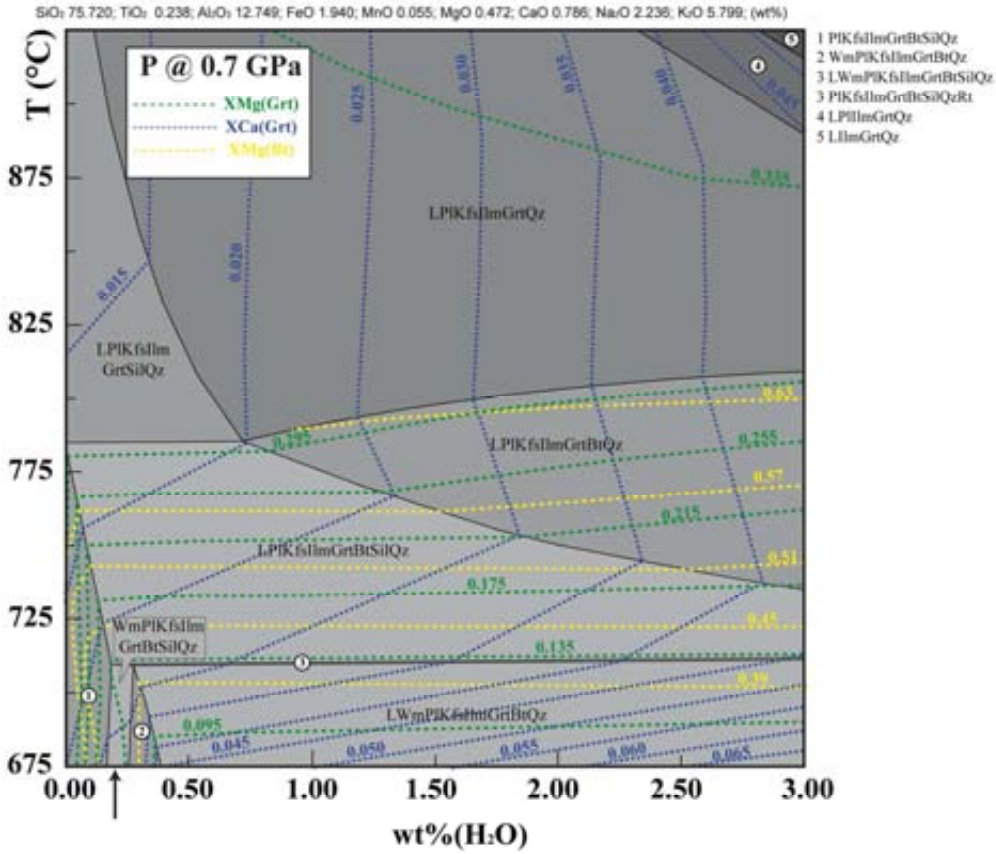

Fig. S6

150x134mm (300 x 300 DPI)

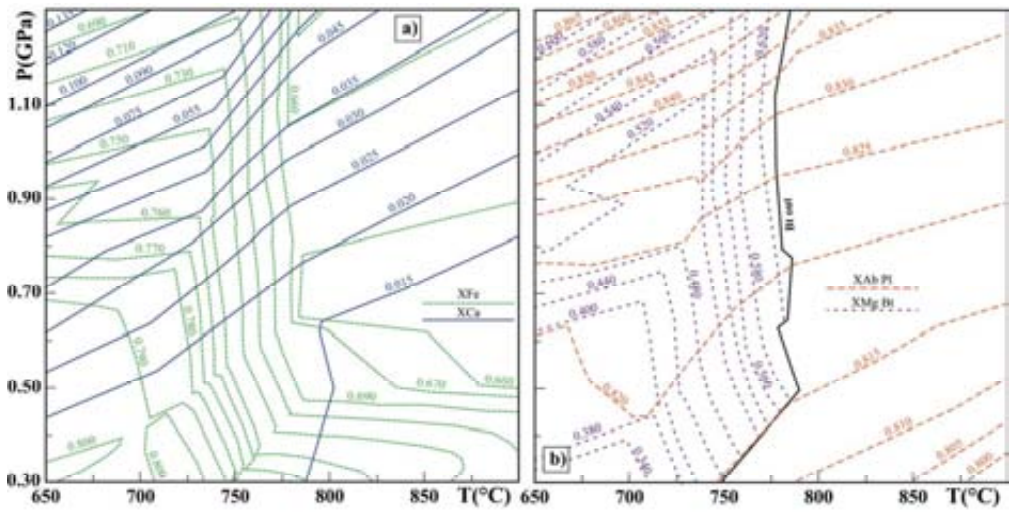

Fig. S7

150x85mm (300 x 300 DPI)

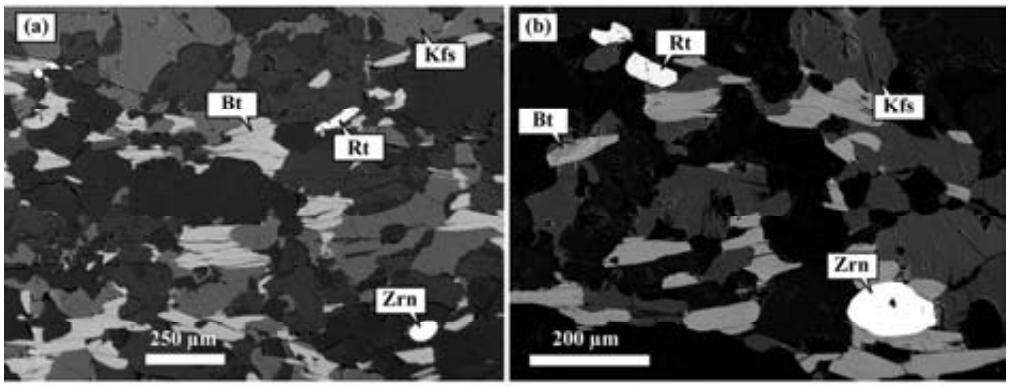

Fig. S8

150x63mm (300 x 300 DPI)